Nanoscale Morphology and Electrical Behaviour of a Pressure Sensitive Ink

WEBB, ALEXANDER,JAMES

Nanoscale Morphology and Electrical Behaviour of a Pressure Sensitive Ink

Alexander James Webb

MSc **2010**

Declaration

I confirm that no part of the material offered has previously been submitted by me for a degree in this or any other University. If material has been generated through joint work, my independent contribution has been clearly indicated. In all other cases, material from the work of others has been acknowledged and quotations and paraphrases suitably indicated.

Signed……

Candidate

The work reported in this thesis was carried out by the candidate. Any work not carried out by the candidate is acknowledged in the main text.

Signed……

Academic Supervisor

Statement of Copyright

Nanoscale Morphology and Electrical Behaviour of a Pressure Sensitive Ink

Alex Webb

Abstract

Pressure Sensitive Ink is an electrically conductive composite material made by Peratech Ltd. The conductivity of the inks is sensitive to touch pressure, which have a range of applications in areas including telecommunications and robotics and are printable as functional electronic devices. The inks are complex and composed of electrically conductive acicular (needle-like) refractory filler particles dispersed in an insulating organic base ink. Inks mixed, prepared and stored in a variety of conditions have been studied using high resolution scanning and transmission electron microscopy, focused ion beam and EDX elemental analysis in conjunction with DC electrical characterization.

The research has aimed to investigate possible links between the structure and electrical behaviour of the inks. The results have shown that inks stored for greater amounts of time, prior to printing, lose touch sensitivity. Causes for this are uncertain, but may be linked with the growth of nanoscale features on the filler particles and partial settling of constituents. EDX analysis revealed candidate elements for the nanoscale features found on filler particles. Modeling current-voltage plots with non-linear fits has shown there might be a switching of conduction mechanism with increasing compression of the inks. Additionally, the unclear process by which inks lose touch sensitivity was shown to be temperature dependent. Inks more vigorously blended were found to have shorter filler particles through a statistical survey of filler particle lengths, measured through scanning electron microscopy imaging. Inks produced with a lower filler particle to base ink ratio were found to be less sensitive to touch pressure than those made with comparatively more filler particles. A survey of

filler particle clumps (groups of 3 or more particles) revealed that the addition of hyper-dispersant, an anti – clumping chemical agent, aided better dispersion of filler particles and increased the touch sensitivity of low filler particle fraction inks.

Contents

Table of Figures

1. Introduction

1.1 Introduction to Chapter

This chapter introduces electrically conductive composite materials, quantum tunnelling composites, the development of pressure sensitive composite inks and finishes by outlining the content of the thesis.

1.2 Electrically Conductive Composites

A composite material, in the context of this research, is comprised of electrically conductive filler particles thoroughly mixed into an electrically insulating medium such as a polymeric material like silicone elastomer.

Conductive composites have been studied for over 50 years [1]. During this time, they have been manufactured using a wide variety of conductive filler materials including nickel and iron powders, carbon nanotubes and most commonly carbon blacks (amorphous carbon). These fillers are then dispersed in an insulating polymer matrix [2 - 4]. Filler particle sizes vary from tens of nanometers to tens of micrometers [5]. The polymers used include polyethylene, polyethylene terephthalate and epoxy resins [5, 6]. Filler geometries vary from amorphous and spherical to high aspect ratio shapes such as flakes and rods [7 - 10].

The electrical properties of composites are dependent upon the stress applied to the material. Compression acts to bring filler particles in the insulating polymer closer together, with further increases in compression leading to direct physical contact with each other. At some level of stress, electrically conductive pathways form through the composite. Several mathematical models have been developed in order to describe the electrical behaviour of composite systems. By far the most

successful and popular are the percolation and effective media models, which are described in detail in chapter 2.

Due to their pressure sensitive nature, composite systems are attractive for applications such as electronic switches, but have been investigated for other applications such as chemical vapour sensing and electrostatic discharge control [11].

1.3 Quantum Tunnelling Composites

Quantum Tunnelling Composite™ is a pressure sensitive material developed in 1996 by Peratech Ltd. The original material comprised of 1 to 10 µm diameter spiky nickel particles dispersed, at a very high concentration, in an electrically insulating elastomeric polymer [12]. The electrical conduction behaviour of this composite is highly sensitive to applied stress, with deformation (compression and torsion) causing the materials' resistivity to drop by several orders of magnitude.

The nanoscale spiky morphology of the nickel particles is key to the materials' behaviour. Such a nickel particle, in Quantum Tunnelling Composite™, is shown in figure 1.1 [12]. Quantum Tunnelling Composite™ uses a nickel powder commonly found in other composites. In traditional composites filler particles are vigorously mixed into the insulating polymer. In contrast, the nickel powder in Quantum Tunnelling Composite™ is gently blended into the polymer. The nickel particles in Quantum Tunnelling Composite™ retain their spiky structure, a property lost by the vigorous mixing used in the traditional composite manufacturing process.

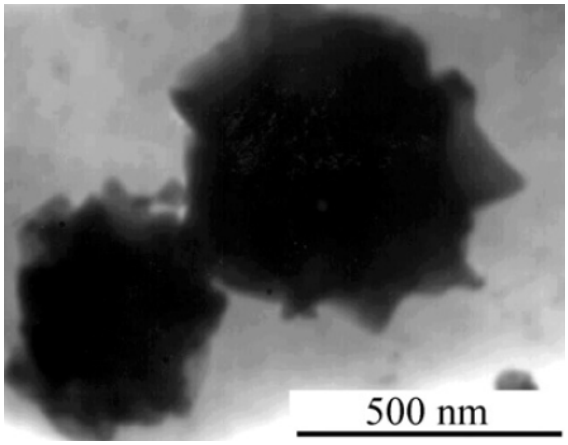

Figure 1. : A transmission electron microscope image of a microtomed nickel particle within a Quantum Tunnelling Composite™ sample. The spiky morphology of the particles is clear.

Previous work on Quantum Tunnelling Composites™ has revealed that, when a bias voltage is applied across a Quantum Tunnelling Composite™ sample, large electric fields develop at the tips of the nickel spikes. Placing the material under compression or tension results in bringing some of these spikes closer together, allowing Fowler-Nordheim (field-assisted) tunnelling of electrons to occur from spike tip to tip [13]. The conduction mechanism is described in more detail in chapter 2.4.

1.4 Application of Quantum Tunnelling Composites

As with other composite materials, Quantum Tunnelling Composite™ has a direct application in pressure sensing and electronic switching, except in Quantum Tunnelling Composite™ the filler particles need not be in direct contact to conduct electricity, greatly increasing the longevity of the material. It is also useful in other applications such as chemical vapour sensing and electrical discharge protection. Some further examples of Quantum Tunnelling Composite™ applications are shown in figure 1.2 [14].

Figure 1. : A depiction of several electronic switch and pressure sensing applications of Quantum Tunnelling Composite™.

1.5 Pressure Sensitive Ink

A new development from Peratech in the area of conductive composites is pressure sensitive ink. The benefit of a composite ink lies with its easy manufacture through printing processes and the potential range of applications.

This particular pressure sensitive ink can be screen printed at varying thicknesses. Screen printing, see figure 1.3, which involves using a squeegee to force ink through a masked mesh onto a substrate, allows the use of nano to micron sized filler particles and can be readily scaled to industrial manufacturing volume.

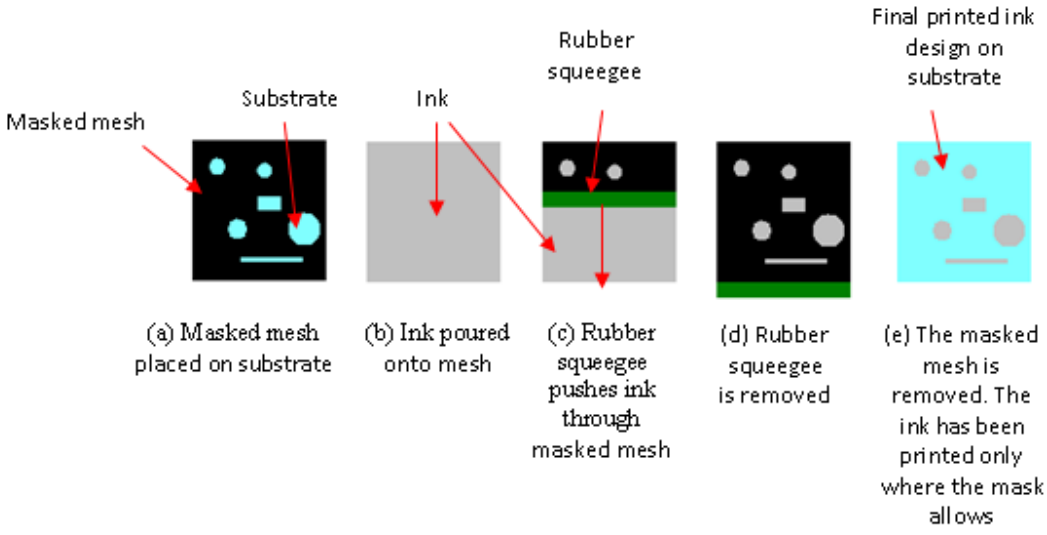

Figure 1. : A schematic diagram showing the stages of screen printing, from (a) to (e).

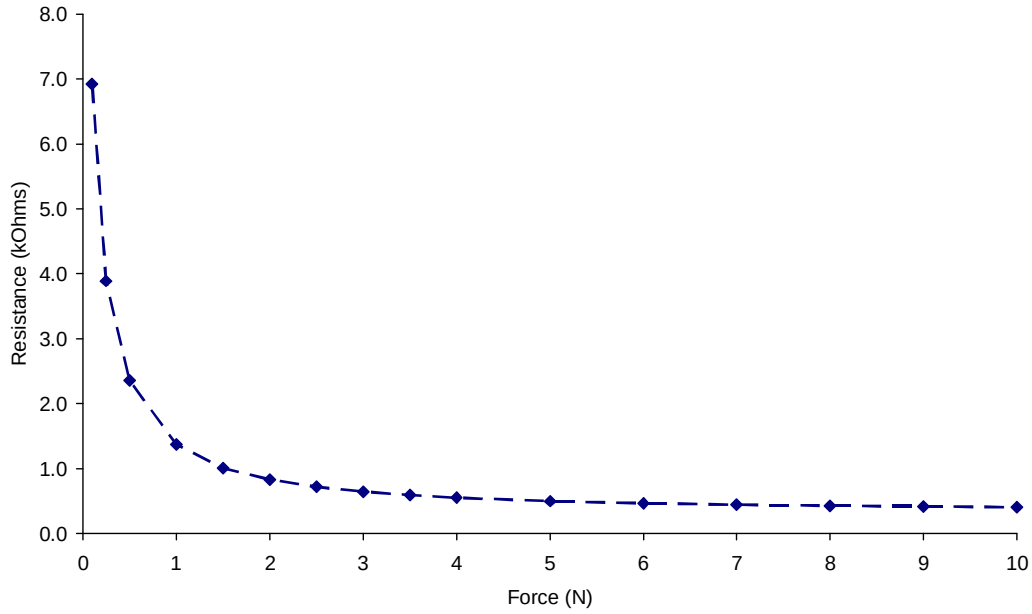

Figure 1. : Example of how the resistance of screen printed pressure sensitive ink falls with increasing applied force. The dashed line is a guide to the eye.

The ink is complex and contains acicular (needle-like), refractory nano-rod filler particles, dispersed in solvent and an organic base ink containing rough "spheres" of a very wide band gap semiconductor (essentially an insulator). Like the original Quantum Tunnelling Composites™, it is highly sensitive to touch pressure; its resistance can drop several orders of magnitude with the application of just 10 N, as shown in the example in figure 1.4.

1.6 Focus, Aims and Motivation

The material focus of this study is the aforementioned pressure sensitive ink. The overall aim of the investigation is to relate the ink's physical structure with its electrical behaviour and to try to understand how the ink preparation processes are related to electrical behaviour by changes in the physical structure.

Several preparation variables are capable of affecting the touch sensitivity of pressure sensitive inks. For example, after mixing filler particles, solvent and base ink, the final pressure sensitivity depends upon blending time and speed, storage time and storage temperature prior to printing. When printed, inks stored for longer periods of time display reduced pressure sensitivity (a firmer press is required to lower ink resistance, compared to a younger ink). If inks are stored in a refrigerator, however, they do not degrade as much as those stored at room temperature.

Additionally, filler particle concentration can alter ink behaviour. Inks made with higher concentrations of conductive filler particles show greater stress sensitivity. Inks made with lower filler concentrations and hyper-dispersant, a solution which combats aggregation and allows better dispersion of particles, exhibit pressure sensitivity that is comparable to inks with higher filler concentrations. All of these issues have been addressed in this investigation.

1.7 Outline of Remaining Chapters

This section briefly details the contents of the forthcoming chapters in the thesis. Chapter 2 contains scientific theory relevant to composites, Quantum Tunnelling Composite™ and pressure sensitive inks. Included are subsections on the percolation and effective media theories, quantum tunneling, charge flow in insulating materials and random resistor networks. Chapter 3 describes the scientific basis for the experimental systems used during the course of the investigation. The chapter begins with a description of sample production and preparation techniques, moving on to discuss the principles and sample specific setups of electrical transport measurements, scanning electron microscopy, focused ion beam, transmission electron microscopy and, finally, atomic force microscopy. The results of the investigation are described and discussed in chapter 4. Lastly, overall conclusions are stated in chapter 5.

2. Background Theory of Conductive Composites

2.1 Introduction

This chapter first discusses the percolation and effective medium theories, two of the most important theories of conductive composites. The focus then shifts to quantum tunnelling and current in insulators, issues which are of more importance to quantum tunnelling composites and pressure sensitive inks.

2.2 Percolation Theory

Percolation theory was introduced in 1957 by Broadbent and Hammersley [15]. It was originally intended to describe how liquid can make its way through a porous material. The material is modelled as a three dimensional (3D) array of independent points. A connection (or hole in the real material) might exist between two points, allowing liquid to flow through. The existence of a connection is assigned a probability, p. The probability of there not being a connection between two points is therefore 1-p. The overall probability of liquid passing through a porous material then depends on p.

This theory can be applied in many different situations, in particular electrical charge flowing through a composite material composed of conducting particles in an insulating matrix. The insulating material is analogous to the porous material in the liquid/porous material model, while the filler particles represent the connections between points in the array. The theory assumes the filler particles are dispersed randomly within the insulating material. The conductivity, σ, of a composite material can be modeled as a function of the volume fraction of conductive filler particles [16]. This is shown in the equation below;

$$\sigma \propto (\phi - \phi_C)^t \tag{2.1}$$

φ is the volume fraction of conductive filler particles. φ_c is the percolation threshold, the critical volume fraction of filler particles at which a conductive pathway through the insulating matrix forms. The value *t* is an exponent which usually takes a value between 1 and 6.27 for 3D systems [3,17,18]. Below the percolation threshold, conductivity rises in a very slow, linear fashion as there is no direct electrical contact from one end of the insulating material to the other. As soon as the volume fraction of the conductive filler particles reaches the percolation threshold, however, a conductive pathway is formed across the insulating matrix. Further increasing the volume fraction of conductive filler particles causes the conductivity to increase dramatically, following a power law. Figure 2.1 shows the conductivity of an example conductive filler-polymer composite as described by percolation theory.

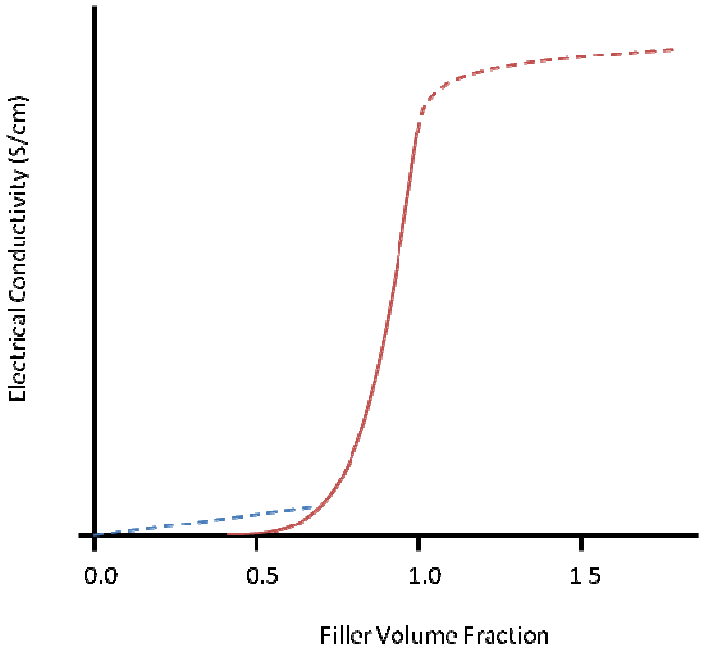

Figure 2. : The ideal change of electrical conductivity with increasing filler volume fraction, as predicted by percolation theory. Here, the critical volume fraction is 0.5 and t=2. The blue dashed line is the ohmic region which percolation theory cannot describe. The red dashed line depicts the area where maximum conductivity is reached.

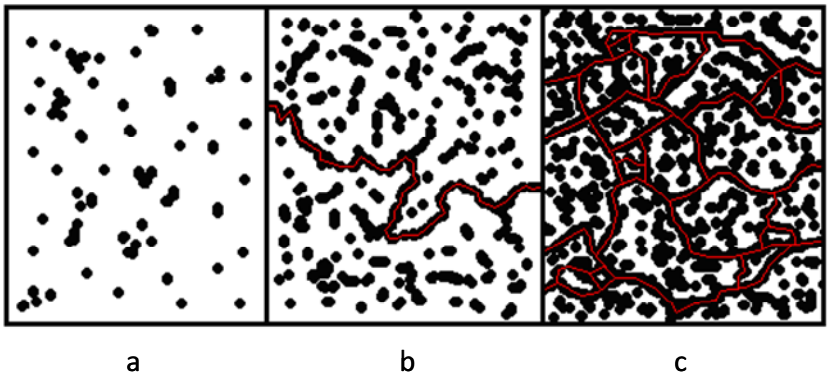

Figure 2. : A diagram showing three stages of conductive filler volume fraction. (a) shows the filler volume fraction below the critical fraction, (b) shows the filler volume fraction equal to the critical fraction and (c) shows the filler volume fraction above the critical fraction. The black dots represent filler particles and red lines are conduction pathways.

Percolation theory can only be accurately used at filler concentrations above the critical volume fraction, and does not describe the transition between insulator and conductor very well, as only minute changes in the volume fraction of conductive filler can cause a dramatic change in composite conductivity [19]. Figure 2.2 describes this process. Figure 2.3 gives a real example of percolation in an expanded graphite and stearine composite [20].

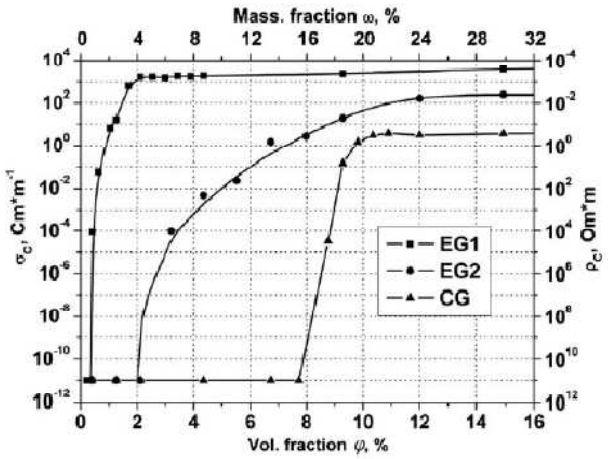

Figure 2. : A diagram of electrical conductivity (left axis) against volume fraction of conductive filler (bottom axis) for two expanded graphite (EG1 and 2) and one crystal graphite (CG) sample.

2.3 General Effective Medium Theory

Effective medium theory (EMT) is a very popular theory used to describe conductive composite materials. The theory is built upon the same fundamental principles as percolation theory [21]. A composite is modelled as a 3D array of random independent points. The points represent the conductive filler particles. Each point has an associated resistance with every one of its nearest neighbouring points. EMT then removes all of the resistances and replaces them with one average value of resistance. This creates a single effective medium which is homogeneous, symmetric and has the overall macroscopic properties of the percolation model of conductive composites. The theory removes the sharp transition from insulator to conductor at the percolation threshold and can more accurately describe the behaviour of the conductivity of a composite at $p \sim p_c$ [19].

From the standard EMT described above, McLachlan devised the General Effective Medium (GEM) theory, which takes into account particle size, shape and orientation contributions to the conductivity of the conductive composite. The equation for GEM is as follows in equation 2.2 [22].

$$\frac{f\left(\sigma_l^{1/t} - \sigma_m^{1/t}\right)}{\sigma_l^{1/t} + A\sigma_m^{1/t}} + \frac{\varphi\left(\sigma_h^{1/t} - \sigma_m^{1/t}\right)}{\sigma_h^{1/t} + A\sigma_m^{1/t}} = 0 \qquad (2.2)$$

where σ_l and σ_h are the conductivities of the low and high conductivity components (insulator and conductor) of the composite, while σ_m is the conductivity of the averaged effective medium. The values f and φ are the volume fractions of the low and high conductivity composite components, and $f + \varphi = 1$ is always true. The exponent, t, is defined by the following equations [11].

$$t = 1/\left(1 - L_f + L_\varphi\right) \text{ For orientated ellipsoids} \tag{2.3}$$

$$t = \left(m_f \times m_\varphi\right)/\left(m_f + m_\varphi\right) \text{ For random ellipsoids} \tag{2.4}$$

where L_f and L_φ are phenomenological constants of the low and high conductivity components of the composite in an oriented ellipsoid case. The value of the constants depends on the shape of the particles, e.g. *L=1/3* if the particles are spheres. The values m_f and m_φ are, likewise, phenomenological constants for a random ellipsoid case. The value, *A*, in equation 2.2 is defined below in equation 2.5 [11].

$$A = \left(1 - \varphi_c\right)/\varphi_c = f_c/\left(1 - f_c\right) \tag{2.5}$$

where φ_c is the critical volume fraction of the high conductivity component that causes the composite to undergo the transition from insulator to conductor. *A* is a ratio of the low conductivity component critical volume fraction (which causes the composite to switch from conducting to insulating) and the high conductivity critical volume fraction. φ_c can be related to the geometry and orientation of the low and high conductivity components through the phenomenological constants introduced in equations 2.3 and 2.4 [11]. These relations are given in equations 2.6 and 2.7.

$$\varphi_c = L_\varphi/\left(1 - L_f + L_\varphi\right) \tag{2.6}$$

$$\varphi_c = m_f/\left(m_f + m_\varphi\right) \tag{2.7}$$

A graph comparing the percolation and EMT fits of composite conductivity is provided in figure 2.4.

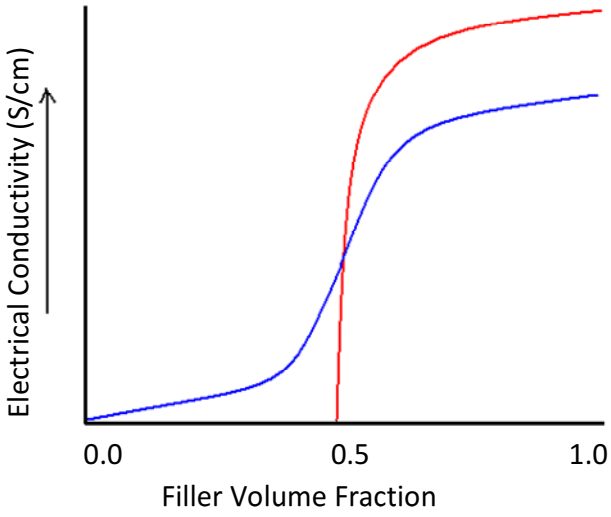

Figure 2. : A comparison of conductivity curves generated by percolation theory (red line) and effective medium theory (blue line) for an ideal composite with a critical volume fraction of 0.5. Effective medium theory can describe the conductivity below the critical fraction/percolation threshold and simulates a more gradual shift from insulating to conducting behaviour [16].

Composites which have been prepared with filler particle volume fractions near or very slightly above the percolation threshold will still have a low conductivity and become highly sensitive to touch pressure. An increase of pressure on the percolation network has the same effect as increasing the filler volume fraction, pushing more of the filler particles into direct contact, completing the composites' dramatic switch from insulator to conductor. Over this transition the dominant electrical properties and conduction mechanisms in the composite change. These may include an increase or decrease in the degree of quantum mechanical tunnelling, charge hopping and charge trapping, depending on the average filler particle separation, geometry and choice of insulating matrix. These transformations can often reveal themselves in current-voltage curves as hysteresis patterns and non-linear behavior. This is a major focus of the work presented in this thesis. As such, the remainder

of this chapter discusses necessary background knowledge of quantum tunnelling, charge hopping and charge trapping.

2.4 Quantum Tunnelling

As the name suggests, quantum tunnelling composite is known for quantum tunnelling being a major contributor to its electrical conduction. Quantum tunnelling can be described as a simple example using solutions of the 2D time independent Schrödinger equation below.

$$-\frac{\hbar^2}{2m}\frac{d^2\Psi(x)}{dx^2}+V(x)\Psi(x)=E\Psi(x) \tag{2.8}$$

$\Psi(x)$ is the wavefunction of an electron; the probability amplitude of finding the electron at position x, $V(x)$ is the potential energy at position x, E is the energy of the electron, m is the mass of the electron and $\hbar$ is the reduced Planck constant.

A simplified situation applicable to the tunnelling occurring in quantum tunnelling composite materials is and electron wave, ψ, of energy E_x, tunnelling through a rectangular potential barrier of thickness b and height V_0. This is shown schematically in figure 2.5, redrawn and modified after [23,24].

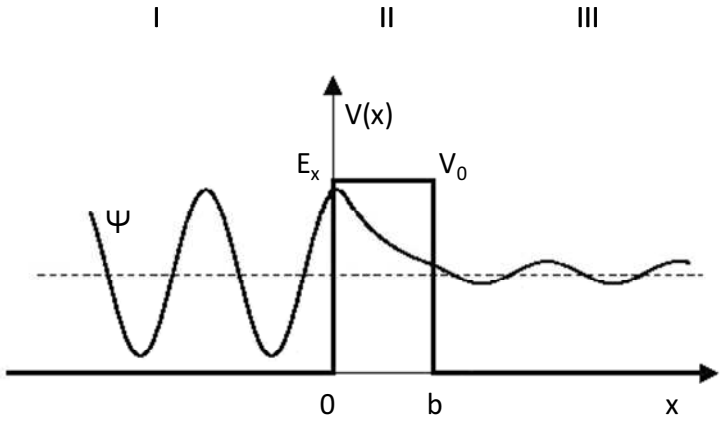

Figure 2. : An illustration of an electron tunnelling through a potential barrier. The regions I, II and III represent the electron wave passing through a conductive filler particle, insulating material and an adjacent filler particle, respectively.

Classically, an electron would reflect back off the barrier at 0. However, in quantum mechanics, there is a finite probability that the electron tunnels through the potential barrier and can be found on the other side. By considering the waveforms in the three regions, I, II and III shown in figure 2.4, one can calculate a transmission coefficient, which is a measure of the probability the electron will pass through the potential barrier [24]. The following equations represent wavefunctions for each of the three regions;

Region I $$\Psi_I(x) = Ae^{ikx} + Be^{-ikx} \tag{2.9}$$

Region II $$\Psi_{II}(x) = Ce^{\mu x} + De^{-\mu x} \tag{2.10}$$

Region III $$\Psi_{III}(x) = Fe^{ikx} + Ge^{-ikx} \tag{2.11}$$

$$where\ k = \frac{\sqrt{2mE_x}}{\hbar}\ and\ \mu = \frac{\sqrt{2m(V_0 - E_x)}}{\hbar}$$

By simplifying the above equations, (recognising that, for example, the coefficients C and G are equal to zero), imposing conditions forcing the wavefunctions to equal each other at the boundaries of the regions and taking the definition of the transmission coefficient in equation 2.12;

$$T = \frac{probability\ of\ \ transmitted\ \ wave\ in\ region\ III}{probability\ of\ \ incident\ wave\ in\ region\ I} = \frac{|F|^2}{|A|^2} \tag{2.12}$$

it is possible to calculate a more detailed transmission coefficient, equation 2.13:

$$T = \tau = 16\left(\frac{E_x}{V_0}\right)\left(1 - \frac{E_x}{V_0}\right)e^{-2\mu b} \tag{2.13}$$

The presence of a large electric field causes Fowler-Nordheim Tunnelling [25, 26]. The electric potential distorts the rectangular potential barrier so that it becomes a narrow, rounded triangle. The distortion is so great that electrons, instead of tunnelling through the barrier to the other side, tunnel through to the conduction band of the insulator (which creates the potential barrier), and then to the material on the far side of the barrier, as shown schematically in figure 2.6, redrawn and modified after [20]. As conduction occurs through the insulator, the electrical properties of the insulator become relevant.

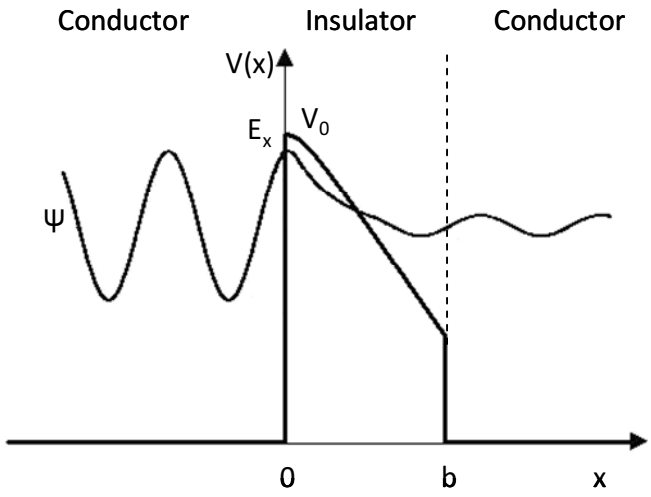

Figure 2. : A schematic illustration of Fowler-Nordheim tunnelling. The presence of a very strong electric field perturbs the potential barrier into a rounded triangle geometry, allowing electrons to tunnel from the conductor to the conduction band of the insulator and then to an adjacent conductor.

2.5 Current in Insulators

When sufficient charge is injected into an insulator, a current can flow through the insulator's conduction band as what is called a space charge [27]. Space charge flowing through an insulator is disrupted and limited by phonon collisions, chemical impurities and structural imperfections, such as dislocations. These impurities and imperfections create charge carrier traps in the insulator. Different chemical species can trap charge by having a higher or lower electron affinity than the rest of the insulator, while crystal defects create vacant states between the conduction and valence bands of the insulator [28]. An electric current passing through an insulator containing impurities displays ohmic behaviour, initially. When a certain current is reached, however, electrons begin to fall into trap sites and do not contribute to the conduction through the insulator. If left in a steady state (constant voltage), the current will gradually increase as trap sites fill up and no longer hamper the flow of conduction electrons. The insulator displays a Space-Charge-Limited-Current (SCLC) when

space charge is being trapped as detailed. In this case, Child's law, given in equation 2.14, is obeyed [19].

$$I = JS = \alpha \frac{SV^{3/2}}{d^2} \tag{2.14}$$

where I is the anode current, J the current density, S the area of the plate, d the distance between the anode and cathode plates and α is a constant of proportionality. The law states that the SCLC varies as the three halves power of the anode voltage in a parallel plane diode. The current continues to rise until all the trap sites are filled, at which point there is a sharp increase in generated current against voltage. This phenomenon is known as the trap-filled limit. If there are many traps at different energy levels within an insulator, there may also be many trap-filled limits [29]. Figure 2.7 shows a current-voltage plot for a SCLC. The section of the curve labelled "b" corresponds to Child's Law.

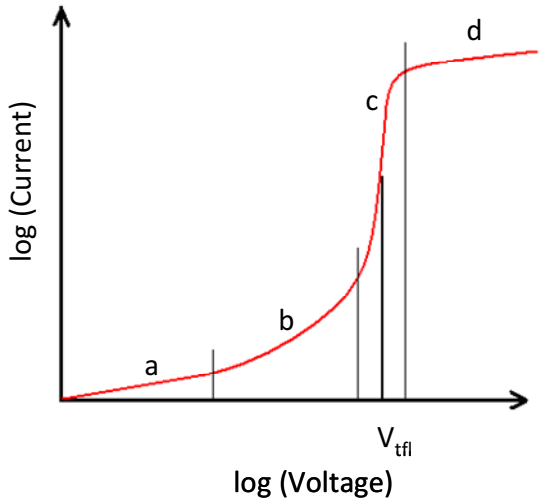

Figure 2. : Schematic illustration of a current-voltage plot of SCLC behaviour in insulators. The conduction regions are described as follows; (a) ohmic regions, (b) Child's law due to shallow trapping, (c) the trap filled limit at V_{tfl} causing a spike in current and (d) Child's law after saturation of traps.

Electron de-trapping can occur either through thermal assistance or the application of a large electric field. A large electric field can narrow and offset the trapping potentials, either completely destroying electron confinement or increasing the probability for electrons to tunnel back into the conduction band. Trapped electrons absorbing phonons can gain enough energy to “hop” over potential barriers into adjacent traps, even if these traps lie at a higher energy level (dependent on the energy acquired from the phonon) [30]. Alternatively, absorbed phonons can allow trapped electrons to tunnel to another trap site of similar energy at a variable distance, hence Variable Range Hopping, as shown in figure 2.7, redrawn after [31].

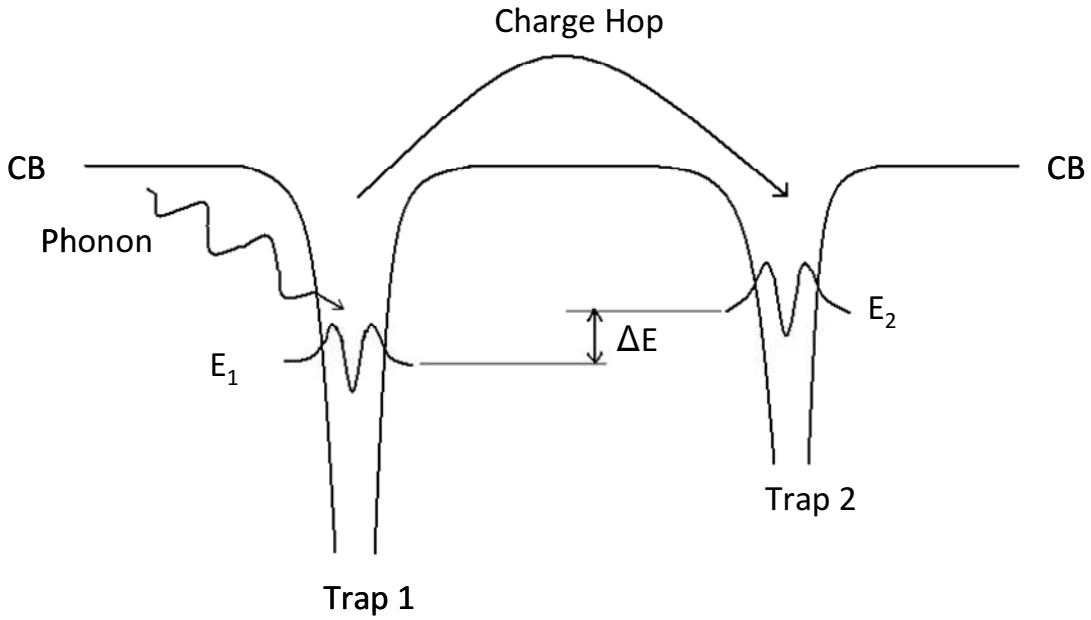

Figure 2. : Schematic illustration of thermally assisted hopping of charge between trapping potentials. In this case, the charge absorbs a phonon to hop to a trap at a higher energy. "CB" indicates the conduction band.

2.6 Random Resistor Networks

Electrically conductive composite materials can often display non-linear current-voltage behaviour [31]. Two phenomenological models are commonly used to mathematically describe this behaviour. The models will be described in the following two subsections.

2.6.1 Non-Linear Random Resistor Networks

The non-linear random resistor network (NLRRN) model assumes that the conducting components of the composite material are microscopic, intrinsically non-linear resistors, distributed randomly throughout the insulating medium and with random orientations [32]. The current-voltage characteristics of each conducting component have a non-linear contribution, such that the relationship between current and voltage for the entire composite material can be described as given in equation 2.15 [33].

$$V = rI + Cl^{a} \tag{2.15}$$

Here, V is the voltage, I and l are the current, r and C are constants and a is an exponent greater than one. For small currents, the behaviour of the composite is considered as being linear. At the crossover current, I_c, where the non-linear conductance is significantly larger than the linear conductance, the current-voltage behaviour becomes non-linear in appearance. The non-linear behaviour described by this model may reflect local heating effects generated by the current applied to composite materials [34].

2.6.2 Dynamic Random Resistor Networks

This model differs from the NLRRN model in that it focuses on a random network of bonds between electrically conductive particles in the composite [35]. Each bond is ohmic in nature, but a certain number of the bonds are initially insulating, able only to conduct above a critical applied external electric field. The non-linear behaviour arising from this model may originate from non-linear hopping and tunnelling of electrons over and through insulating potential barriers [34].

Alternatively, as demonstrated by Chakrabarty et al [35], the current, *I*, can be written as shown in equation 2.16.

$$I = G_1 V + G_2 V^2$$
$$I = V\left(G_1 + G_2 V\right) \tag{2.16}$$

Where G_1 and G_2 are the linear and non-linear conductance, respectively and *V* is the applied voltage.

The precise causes of non-linear behaviour are unclear [32], although recent research has indicated, at least in the case of a carbon nanofibre filler/high density polyethylene composite, that the linear conductivity is attributed to electrical conduction through the conducting network of the composite system, while the non-linear conductivity corresponds to internal field emission and various quantum tunnelling processes between isolated clusters and aggregates of conductive filler material [36].

2.7 Summary

Electrically conductive composite materials have been widely described and modeled with Percolation and Effective Medium theories. These theories can detail the often dramatic changes in

composite conductivity as the volume fraction of conductive filler material is increased from below and to above the Percolation threshold, whereby an electrically conductive pathway forms through the composite as a result of direct physical contact between filler particles. Composites made with filler concentrations just above the threshold retain a low electrical conductivity and can become exceptionally sensitive to the application of touch pressure. These composites can be pushed into a highly conductive state with deformations such as compression from an applied unilateral force. During this transition, conduction mechanisms within the composite may vary and include a mix of direct contact, field assisted quantum tunnelling, SCLC and charge hopping.

3. Experimental Techniques

3.1 Introduction

This chapter describes the background scientific knowledge, principles and techniques associated with preparing the pressure sensitive ink samples, performing electrical transport measurements and structural analysis using a combination of scanning/transmission/atomic force microscopy and focused ion beam.

3.2 Sample Preparation

3.2.1 Ink

Pressure sensitive inks were prepared using the processes outlined in figure 3.1.

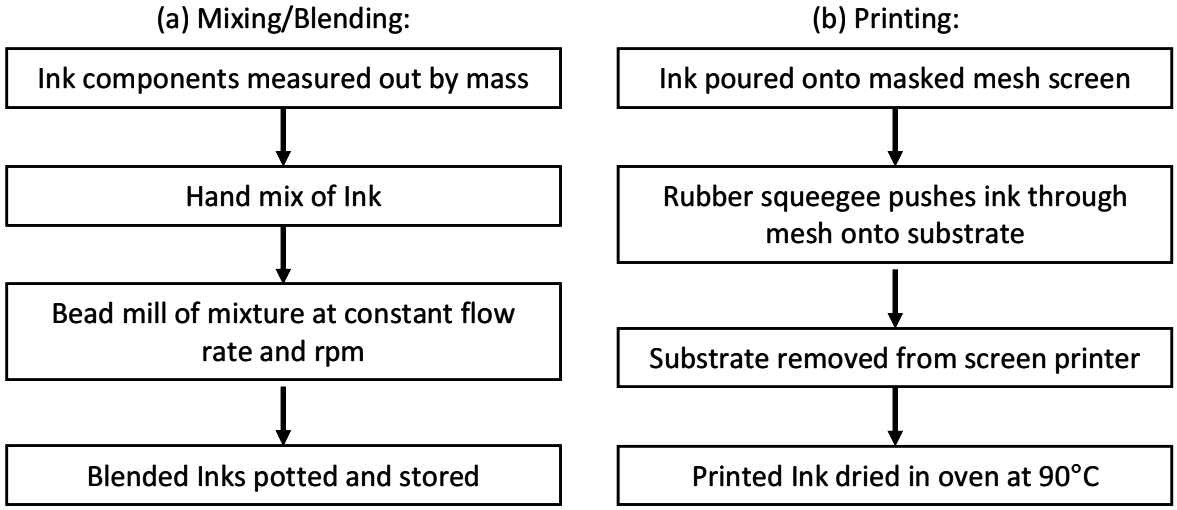

Figure 3. : Flow charts briefing the overall manufacturing process of pressure sensitive ink (a) and printed ink functional electronic pressure sensors (b).

Samples of different storage time (i.e. inks left to stand for varying amounts of time before printing in stage 4 of figure 3.1a), different constituent ratios (i.e. different volume/mass fractions of acicular filler added during stage 1 of figure 3.1a) and samples stored under different conditions (i.e. two identical samples stored for the same amount of time, one kept refrigerated at 4°C, the other kept at room temperature) were printed for analysis. The pressure sensitive inks were printed as functional electronic pressure sensors.

3.2.2 Printing and Structure of Pressure Sensitive Ink Test Pads

The functional electronic pressure sensors were produced as shown schematically in figure 3.2.

A silver conductive track and carbon black contact pad, with a total thickness of approximately 6 µm, is printed first onto a PET (Polyethylene terephthalate) sheet. Next, a ~10 µm layer of pressure sensitive ink is printed on top. On a complementary PET sheet, an additional silver track and carbon black contact pad is printed. The two sheets are then brought together, forming the complete sensor, as shown in figure 3.3.

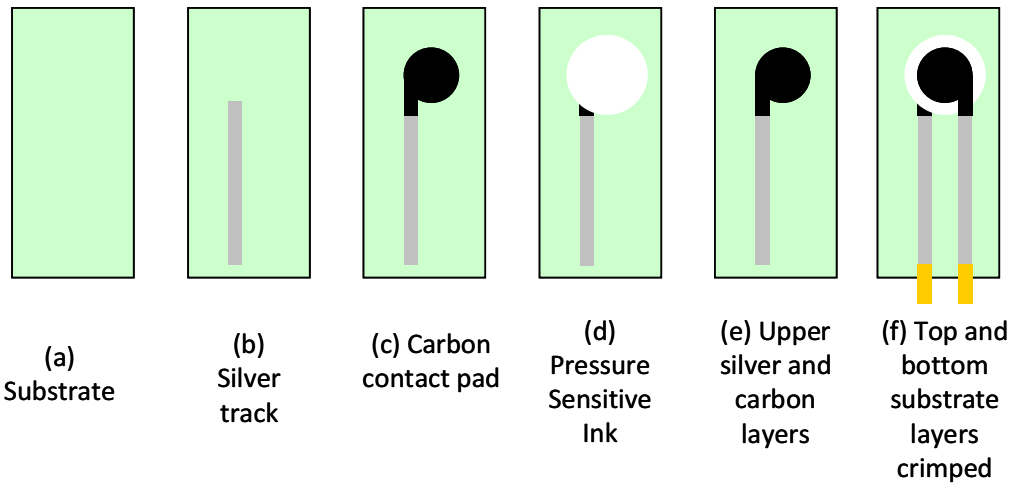

Figure 3. : A schematic series of diagrams showing the stages of the printing of the pressure sensors. (a) Start with blank PET substrate. (b) A silver contact track is printed. (c) Carbon contact pad is printed. (d) Pressure sensitive ink layer is added. (e) A silver track and carbon contact pad is printed on a complimentary sheet of PET. (f) The two sheets are brought together and crimped with external, gold plated contacts.

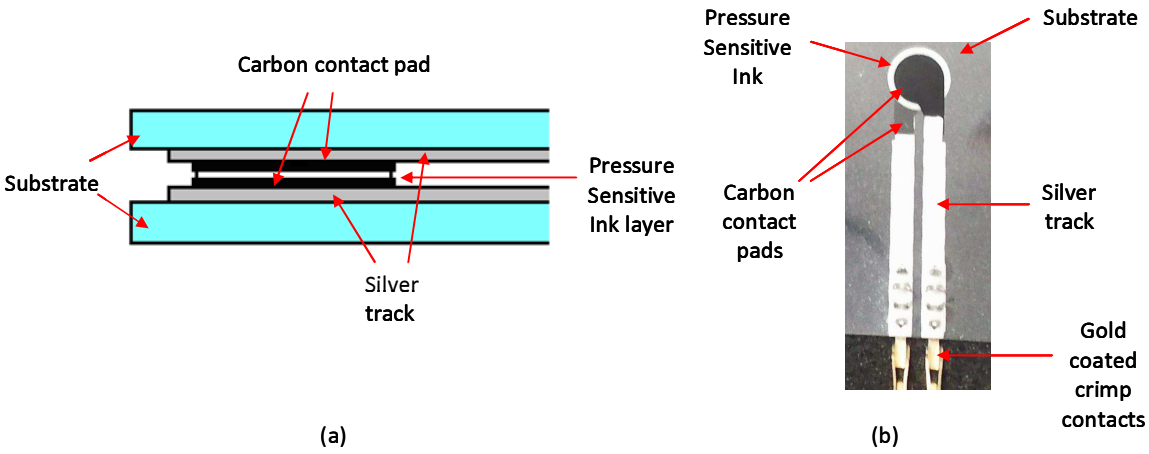

Figure 3. : (a) Schematic cross-section of a pressure sensitive ink sensor, (b) As prepared pressure sensitive ink sensor with contacts.

3.3 Electrical Transport Measurements

3.3.1 Principles

The purpose of this section of the investigation is to attempt to investigate the transport behaviour to understand the conduction mechanisms and any charge trapping phenomena present in pressure sensitive inks. The samples were investigated using current-voltage sweeps. Current was measured as the voltage across an ink sample was steadily increased up to a maximum value. A linear plot is indicative of ohmic behaviour, but a non-linear curve of current against voltage and hysteresis may suggest the presence of more exotic conduction mechanisms. For example, the original quantum tunnelling composites have been shown to exhibit highly non-linear current-voltage behaviour with significant hysteresis, as shown in figure 3.4 [13]. This behaviour was attributed to Fowler-Nordheim tunneling of electrons from nickel tip to nickel tip, charge trapping and the pinching off of conductive pathways by the trapped charge [13].

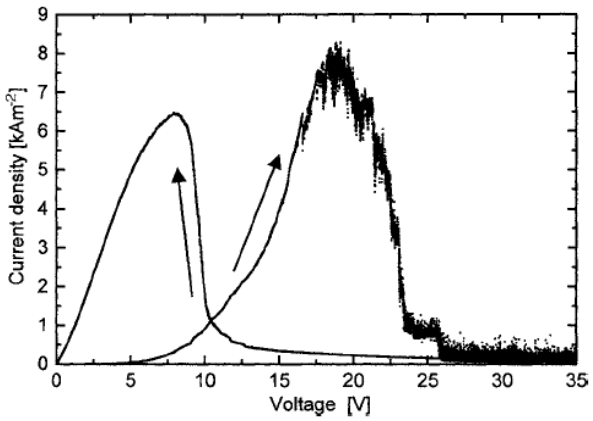

Figure 3. : Current-Voltage behaviour of a Quantum Tunnelling Composite™ pill sample compressed to an initial resistance of 26 kΩ. The current initially rises at 10V non-linearly as a result of field induced tunneling and filling charge traps, which no longer affect conduction electrons as they are filled. At 18V, the amount of charge in trap sites pinches off conduction pathways, causing the current to drop. The small jumps of current are attributed to charge redistribution between traps. Upon decreasing the voltage, some of the trapped charge leaks away.

3.3.2 Experimental System

The electrical transport measurements were undertaken using the system shown schematically in figure 3.5.

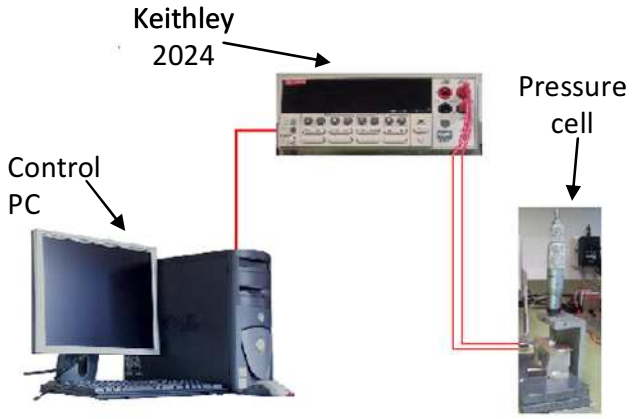

Figure 3. : Illustration of the experimental setup for electrical transport measurements of pressure sensitive inks.

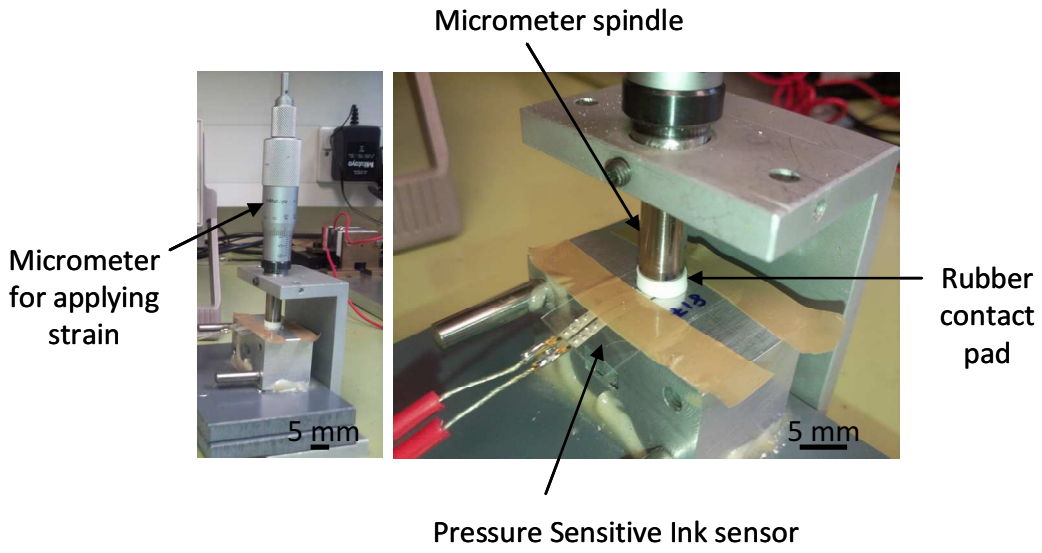

Figure 3. : The pressure cell used to apply uni-axial force to pressure sensitive ink sensors.

Pressure sensitive ink samples with soldered contacts were connected to a multimeter current source, a Keithley 2024. The Keithley meter was, in turn, connected to a PC and controlled using LabView software. The ink sensor was placed in a custom built pressure cell, constructed from the spindle of a micrometer and a rubber contact pad. The pressure cell is shown in figure 3.6. The rubber pad was added as a shock absorber, as the pressure sensors were very sensitive to external knocks, and to decrease the amount by which the resistance of the sensor drops during the relaxation time. When an Ink sensor is brought under compression, the resistance falls rapidly, but needs time (i.e. relaxation time) to settle to a constant value. Figure 3.7 shows how the resistance of a sensor varies under a constant compression with time. This is explained in more detail in section 4.7. The applied voltage was increased from 0 V up to 10 V and back down to 0 V, in steps of 0.1 V. This cycle was repeated 10 times for each ink sensor.

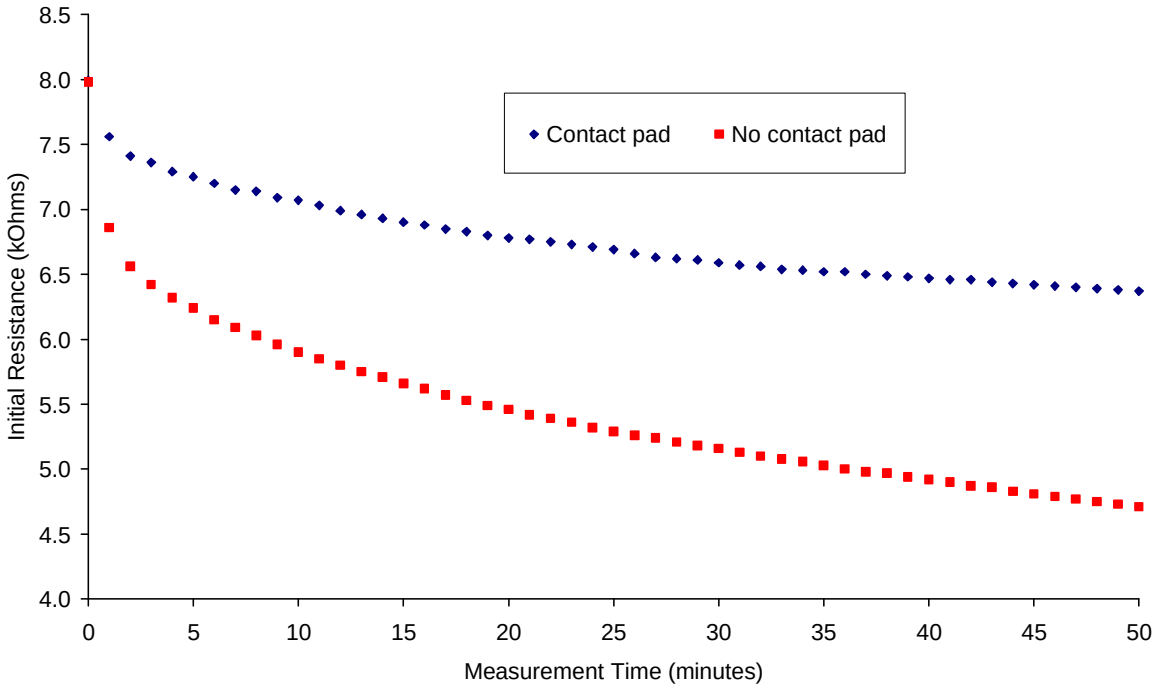

Figure 3. : Graph showing the settling of resistance when an ink sensor is initially brought under compression. The blue data points are from an ink sensor compressed with aid from a rubber contact pad. The red data points are from an ink sensor directly compressed with a micrometer spindle. Error bars are smaller than the data points.

3.4 Structural Analysis of Printed Inks

3.4.1 Scanning Electron Microscopy

3.4.1.1 Principles

The scanning electron microscope (SEM) is one of two main types of electron microscope. It forms images of surfaces by scanning a beam of electrons over a surface in a raster pattern and detecting the intensity of electrons from the sample surface at each pixel. Figure 3.8 is a schematic diagram of a typical SEM, redrawn and modified after [37]. SEMs traditionally use thermionic emission electron sources, although more advanced and modern systems use field emission electron guns as a source of electrons.

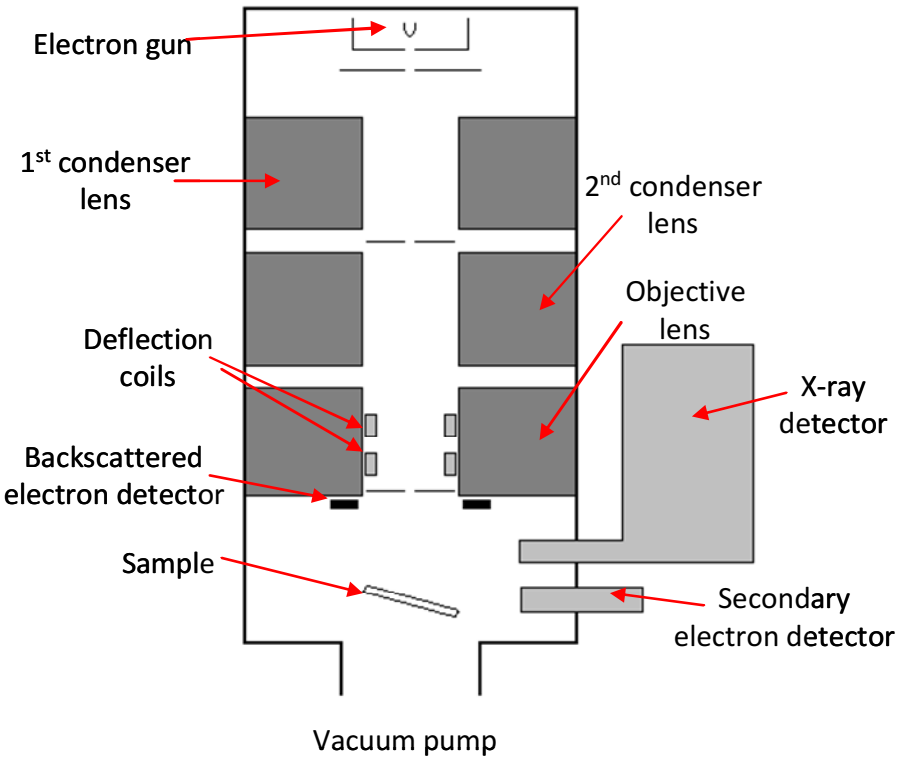

Figure 3. : A schematic diagram of a Scanning Electron Microscope (SEM).

Most thermionic sources are constructed from a filament of tungsten. Tungsten is used because of its low vapour pressure and high melting point. The filament (cathode) is heated up, giving electrons enough energy to stream off the surface of the tungsten, and are accelerated away towards the anode. The use of field emissions guns allows SEMs to create beams of electrons with a higher current density and smaller diameter, which acts to vastly improve the spatial resolution of the microscope. Field emission guns come in varieties, cold cathode or Schottky. The cold cathode type does not need to be heated to operate. The Schottky field emission gun utilises a sharp tungsten tip coated in zirconium oxide. The tip is heated and held at a large negative potential relative to an electrode nearby, which lowers the potential barrier electrons need to cross to be emitted.

Electrons streaming from the electron gun must now be focussed to a very small spot size, commonly around 0.5 to 5 nm, depending on what is being imaged and what resolution is required. The beam of electrons passes through condenser lenses, which are electromagnets, in order to be collimated and condensed to a small beam diameter, taking advantage of the Lorentz force.

The beam then passes through one final lens, the objective lens, another electromagnet, and through a system of scan coils and deflector plates which are used to scan the beam, in the x and y planes, over an area of the sample surface in a raster pattern (the beam position follows a saw tooth wave pattern across the sample area). Magnification is achieved by scanning the beam across a smaller area.

Incident electrons from the beam strike and penetrate the surface of a sample, interacting with it both elastically and inelastically. Elastic collisions cause the incident electrons to back scatter back out of the surface. Inelastic collisions are more complicated, causing secondary and auger electron emission and the production of X-rays.

All of these processes occur within a generation volume, which is most accurately calculated using Monte Carlo simulations. The size of the generation volume is dependent on the energy of the incident electrons. Higher energy electrons will result in deeper penetration and a larger interaction volume. Illustrations of the generation volume and its dependence on beam electron energy and sample atomic number are provided in figure 3.9 [37,38].

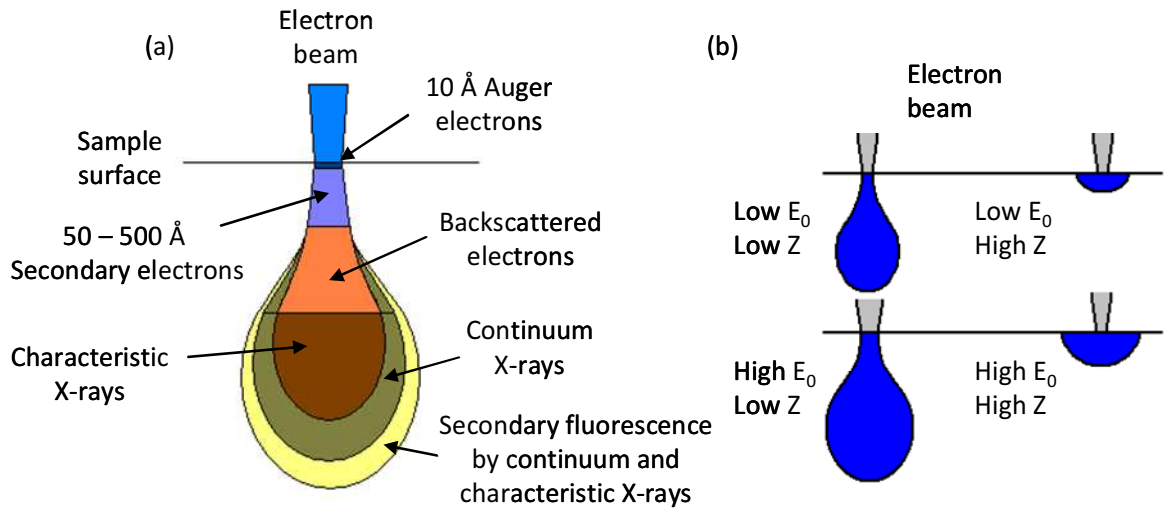

Figure 3. : Schematic illustrations of (a) The generation volume of electron interactions and (b) the dependence of the generation volume size on beam energy and atomic mass.

Backscattered primary (beam) electrons are those that are elastically scattered by the sample. Secondary electrons are the result of ionisation processes caused by inelastic scattering of the incident electrons. Because of the way backscattered and secondary electrons are produced, they have different energies. Backscattered electrons typically have high energy and depend upon the atomic number of the sample (i.e. heavier samples produce a higher intensity of backscattered electrons). Secondary electrons, however, tend to have much lower energies. Figure 3.10 shows an example spectrum of electrons emanating from a sample surface being probed by an electron beam, redrawn after [37,38]. An incident electron collides with an orbital electron in an atom. The incident electron transfers some kinetic energy to the orbital electron, which can now escape its atom (it now has energy exceeding the ionisation potential). Figures 3.11a and 3.11b show the processes by which secondary and backscattered electrons are produced, respectively. The energy of a secondary electron is given below in equation 3.1.

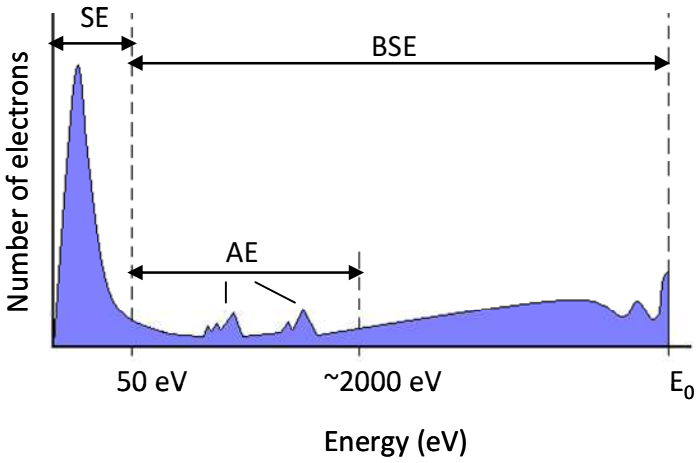

Figure 3. : Schematic diagram of the spectrum of electrons emitted from samples during SEM analysis.

$$E_{kin}^{b} = E_{kin}^{a} - E_{bind}^{b} \tag{3.1}$$

where E_{kin} is kinetic energy and E_{bind} is the binding energy. The superscripts denote the electron, *a* being the beam electron and *b* the atomic, or secondary electron.

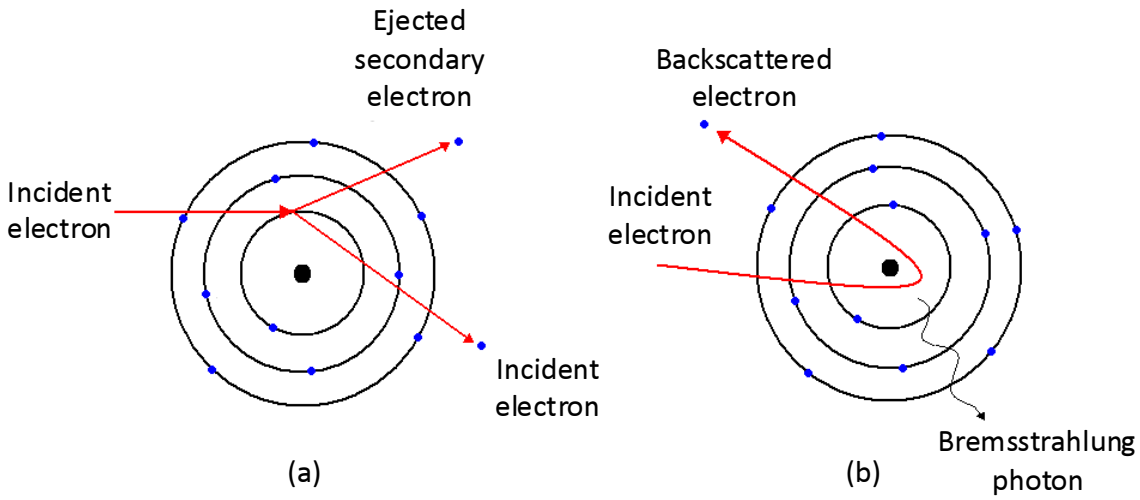

Figure 3. : Schematic illustrations of (a) production of secondary electrons and (b) production of backscattered electrons.

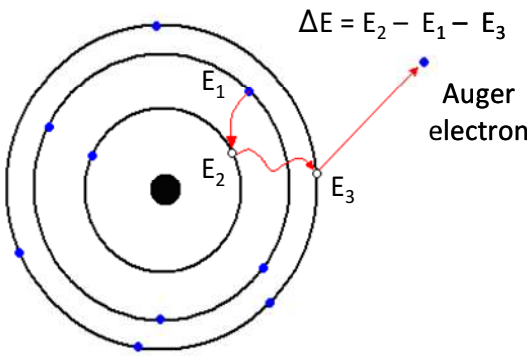

Figure 3. : Schematic illustration of the process responsible for Auger electron emission.

Auger electron emission occurs when, after an ionisation event, an electron from a higher shell falls to a lower shell. The energy released by this transition is immediately absorbed by another electron in the atom, and subsequently escapes. The process is demonstrated in figure 3.12.

X-rays are emitted from the sample due to beam electron deceleration within atoms and after ionisation events. Incident electrons can be slowed by interacting with the electromagnetic field of an atomic nucleus, shown in figure 3.11. As the electron decelerates, it loses energy, emitting a photon. The energy lost, or energy of the photon is dependent on the degree of deceleration. As such, a background continuum of X-rays is produced by this mechanism, called “Bremsstrahlung”. The spectrum of Bremsstrahlung radiation is shown below in figure 3.13.

X-rays emitted from the sample after ionisation events also contain information about which atoms they originated from. Electronic transitions occur at specific energies. Each transition is unique, and so atoms have characteristic X-ray emission lines from electron transitions to vacant core levels. By collecting these X-rays, it is possible not only to identify what elements are present in a sample, but even, to some degree (generation volume), locate where these elements are.

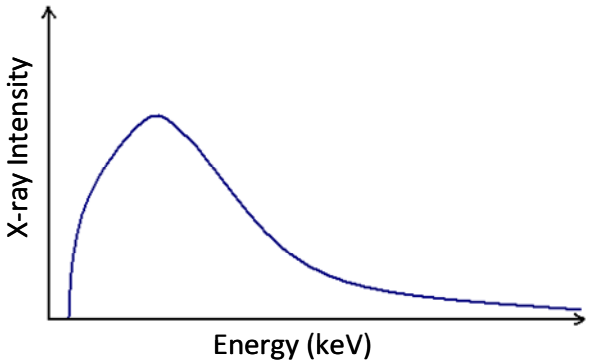

Figure 3. : Illustration of a Bremsstrahlung radiation spectrum.

Moseley's Law, which empirically shows the dependence of x-ray frequency on atomic number, is given in equation 3.2 below.

$$\sqrt{\nu} = C(Z - \sigma) \tag{3.2}$$

where ν is the x-ray frequency, C is a constant, Z is atomic number and σ is a screening factor.

Ionisation occurs when a beam electron interacts with a core electron and ejects it from the atom. An electron from a higher shell may then fall into the empty state. The electron loses energy as it does so, this energy being equal to the difference of the binding energies of the two shells. Thus, a photon of this energy is emitted by the electron. The process is displayed in Figure 3.14, and the energy of the photon is given in equation 3.3.

$$h\nu = E_{b1} - E_{b2} \tag{3.3}$$

where $h\nu$ is the photon energy and E_{b1} and E_{b2} are the binding energies of the inner, ionised level and the outer level from which an electron falls, respectively.

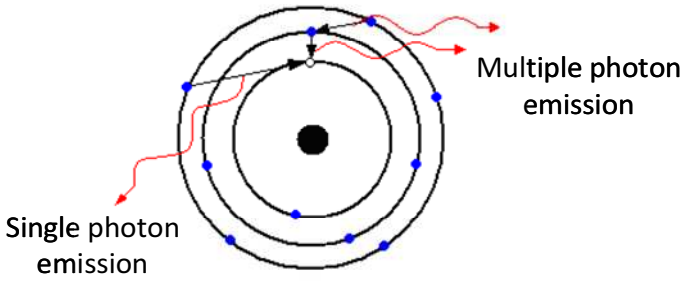

Figure 3. : Schematic illustration of how ionised atoms may produce X-ray radiation.

Given that they have very different energies, different detectors are used for secondary and backscattered electrons. For example, an Everhart Thornley detector is often used for detecting secondary electrons, as shown in figure 3.15 [37,39]. The bias voltage on the Faraday cage attracts the low energy emitted electrons, which are then accelerated to the scintillator, and then to a photomultiplier.

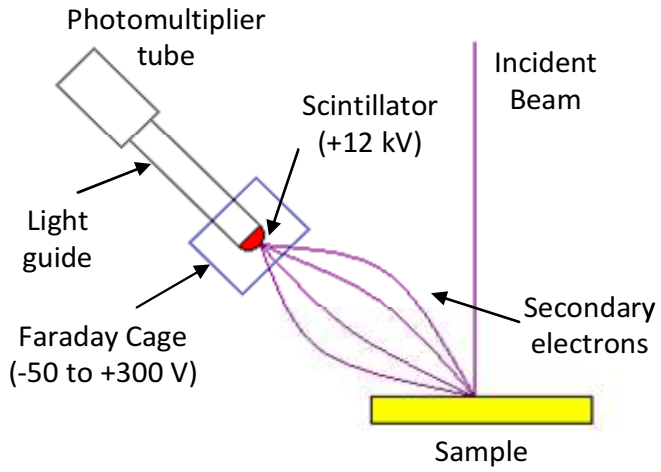

Figure 3. : Schematic illustration of the primary components of an Everhart Thornley secondary electron detector.

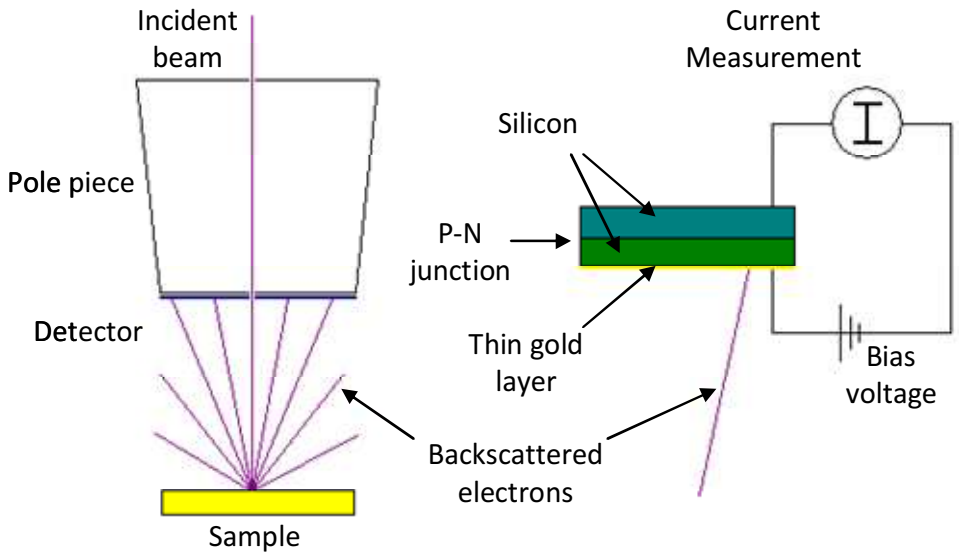

Figure 3. : Schematic illustration of the primary components of a backscattered electron detector.

A silicon p-n junction can be used to detect backscattered electrons (BSE). The detector is housed directly above the sample, as most of these electrons are scattered to high angles, as shown in figure 3.16 [37,39]. Image contrast in BSE images is proportional to atomic number. Heavier elements/atoms are more effective at scattering electrons, and so appear brighter than lighter elements, giving atomic number contrast.

Energy Dispersive Analysis of X-rays (EDX) was also used in this investigation. This method of spectroscopy uses a Si(Li) p-i-n diode, under reverse bias as a detector. This is more commonly known as a Silicon Drift Detector. X-rays incident on the diode generate electron-hole pairs. The amount of energy needed to create such a pair is known exactly for silicon (about 3 E_g, which equates to 3.8 eV). This generates charge pulses. The amount of charge per pulse is related to the energy of the incident photon, and the number of charge pulses depends on the number of photons striking

the detector. The detector is placed in vacuum and cooled by liquid nitrogen or by thermoelectric (Peltier) cooling, which reduces thermal noise. X-rays enter the detector through a thin Beryllium window. Charge pulses from the detector are fed to a Multi-Channel Analyser (MCA), a schematic of which is shown in figure 3.17 [40]. The charge pulses have heights corresponding to incident photon energy and, ideally, different elements. The MCA records the heights of the charge pulses in parallel, which arrive randomly, and bins them in a histogram, which forms the resultant spectrum. Two issues to consider with X-ray analysis are photon energy and the generation volume. The fact that the X-rays are emitted within the generation volume means that you get spectroscopic information from the surface and the material below the surface. This can cause problems for elemental mapping. Also, if X-rays are not very energetic, they will be absorbed by the Be window, which limits the lowest energies that can be observed. However, if they have too much energy, they will simply pass through the detector. Figure 3.18 shows how detection efficiency varies with X-ray energy [40].

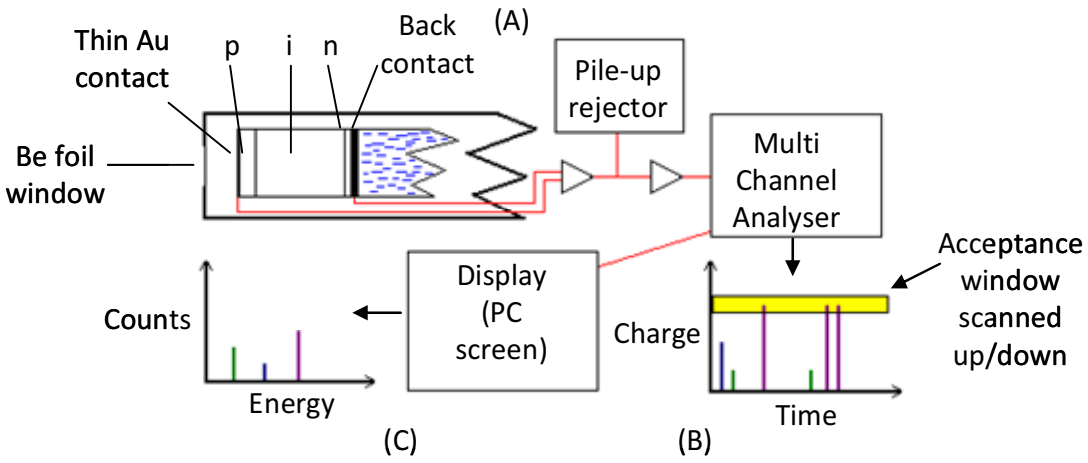

Figure 3. : Schematic diagram of a multi-channel analyser. (A) X-ray signals are detected and sent through a pile-up rejector so one charge pulse is recorded at a time. (B) An acceptance window determines amount of charge per pulse and pulse frequency. (C) Results displayed on computer.

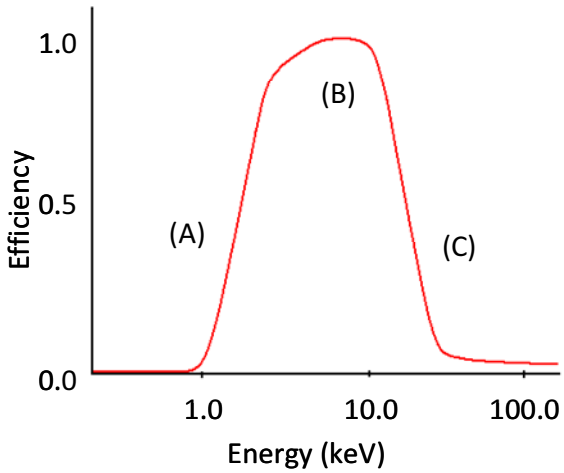

Figure 3. : Schematic illustration of the detection efficiency of X-rays. (A) Low efficiency due to X-ray absorption in Be window. (B) Maximum efficiency. (C) Low efficiency due to high energy X-rays transmitting through entire detector.

3.4.1.2 Experimental System

A Hitachi SU70 SEM, shown in figure 3.19, was used extensively during this investigation [41]. The SEM utilises a Schottky Field Emission electron source, which can achieve a maximum 100nA probe current. It has a maximum magnification of 8.0 x 10^5X and an ultra high resolution of 1 nm at 15 keV beam energy. Additionally, the SEM has EDX and WDX (Wave dispersive x-ray spectrometer) detectors, and the capability to generate ultra-low landing voltages (i.e. slow the beam electrons prior to striking the sample surface), allowing very shallow surface studies.

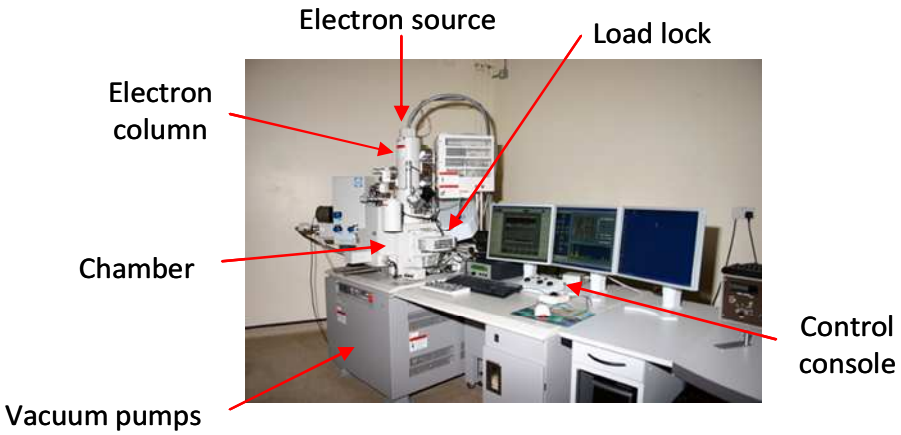

Figure 3. : Image of the Hitachi SU70 Scanning Electron Microscope.

The Hitachi Su70 in figure 3.19 has a load lock mechanism, indicated with an arrow. Aluminium sample stubs are locked into a sample holder which feeds into a side chamber pumped to rough vacuum. Once the side chamber is pumped out, the load lock can be opened, and the sample inserted into the SEM chamber, which is maintained at high vacuum. Once inside the main chamber, the distance between the sample and electron beam column pole piece (working distance) can be adjusted for imaging or EDX analysis. Most of the images of pressure sensitive ink surfaces have been taken at a working distance of 2-7 mm. Generally, accelerating voltages of 8 to 10 kV have been used for the investigation. This voltage was chosen after some experimentation with system settings to find a combination that produced the sharpest images. For EDX studies of the inks, a working distance of 15 mm was used, because of the position of the detector. An incident electron beam of 10keV was chosen to excite characteristic X-rays of up to ~10 keV.

3.4.2 Focused Ion Beam

3.4.2.1 Principles

Focused ion beam (FIB) systems utilise a focused beam of gallium ions to locally sputter material from samples, allowing micro and nanoscale milling which can be used for cross sectioning for imaging purposes [42]. A beam of, typically, gallium ions (Ga^+) is produced by a hot tip of tungsten with liquid Gallium and applying a large electric field, ionising the gallium and field emitting ions. The ions are accelerated from the tip and focused into a beam, using the same principles explained for the SEM and TEM. The ion beam incident on the surface sputters atoms from the surface of the sample, as depicted in figure 3.20 [43]. Here, the FIB was not used to create elaborate patterns or devices, but simply to create cross sections through selected pressure sensitive ink samples in order to investigate the depth profile of the printed inks.

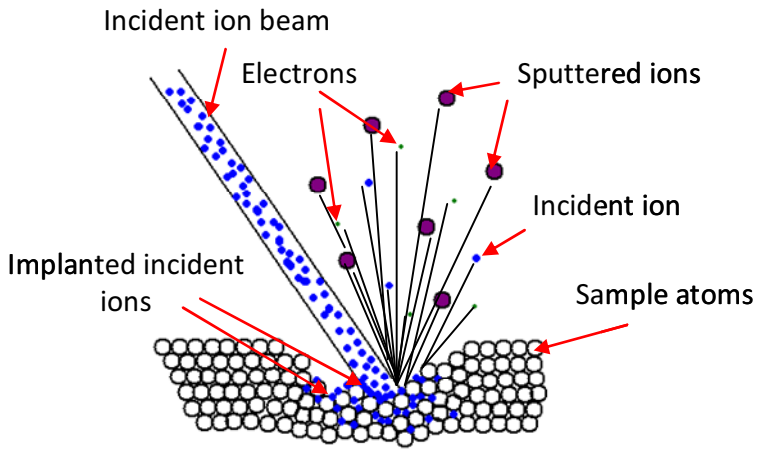

Figure 3. : Schematic illustration of focused ion beam sputtering of a sample surface. Incident ions strike the sample surface, ejecting atoms and ions from the sample. Some of the incident ions implant in the surface.

3.4.2.2 Experimental System

The FEI Helios Nanolab Dualbeam 50 series, displayed in figure 3.21, houses a Schottky field-assisted source electron beam column for extreme high resolution imaging (0.8 nm at 15 keV beam energy) and a Gallium liquid metal ion source ion column for sample milling/etching/fabrication purposes [41]. It was used to etch 14 µm deep, wedge shaped wells in order to view detailed cross sections of printed ink samples.

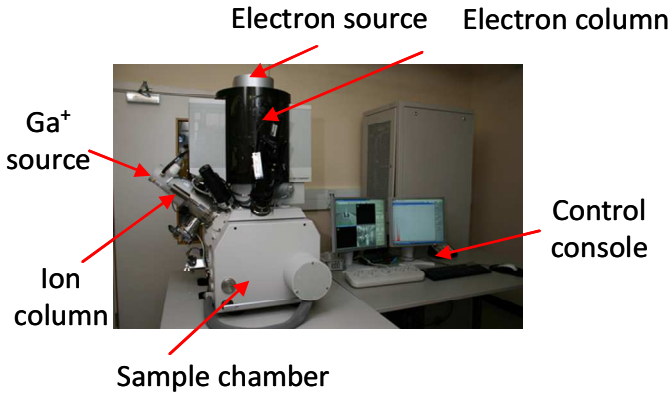

Figure 3. : An image of the FEI Helios Nanolab Dualbeam Focused Ion Beam facility. This particular FIB has both an electron column for high resolution imaging and an ion column for sample milling and manipulation.

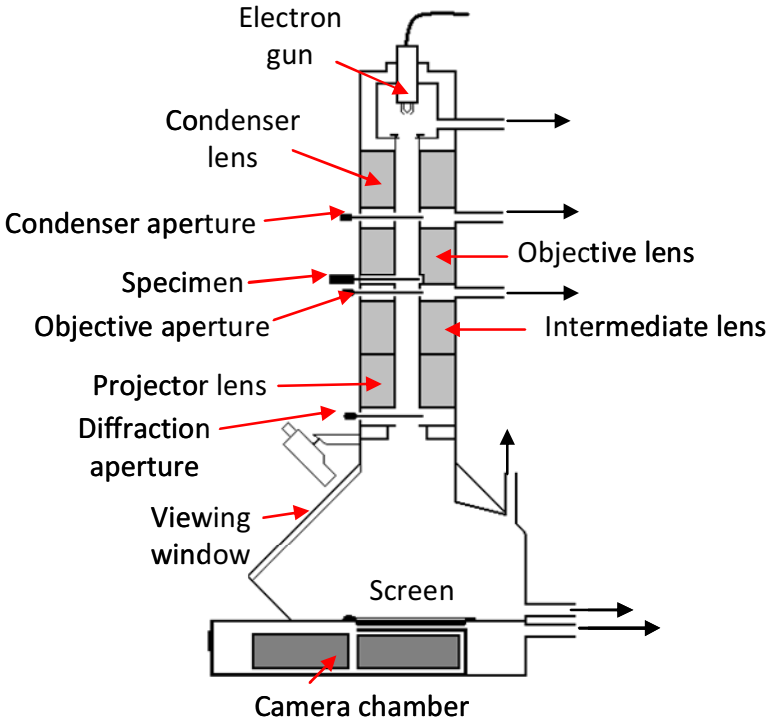

Figure 3. : Schematic diagram of a typical transmission electron microscope. The black arrows indicate connections to vacuum pumps.

The wells were made with 2 cuts. The first "rough" cut was made with a 20 keV ion beam energy and an ion current of 0.6 nA. The "final" cut, at the same energy, but with a much smaller current of 56 pA was performed to clean up the edges of the well to allow accurate and precise imaging. The FIB also has an EDX facility attached.

3.4.3 Transmission Electron Microscopy

3.4.3.1 Principles

A schematic diagram of a typical TEM is given in figure 3.22 [44]. Electrons are produced at the top of the system by a thermionic or Schottky field emission source (often a tungsten filament), acting as a cathode. The source is biased to a very high voltage, as mentioned above, and electrons are

extracted from the tip of the source. The extracted electrons are accelerated downwards by an anode, and are then focused by an electromagnetic condenser lens and shone through the sample being studied. The electrons are subsequently focused again by objective and intermediate lenses, before passing through the projector lenses to form an image on a CCD detector or phosphor screen at the bottom of the microscope. The strength of the lenses can be adjusted so that either an image or the diffraction pattern of electrons passing through the sample is formed on the detector [45].

Images can be formed either through diffraction contrast or phase contrast techniques (for high resolution imaging). Diffraction contrast is achieved through Bragg diffraction of electrons in the sample. Bragg's law of diffraction is given in equation 3.4.

$$n\lambda = 2d\sin\vartheta \tag{3.4}$$

where n is an integer, λ is the wavelength (of an electron in the case of TEM imaging), d is the inter-planar spacing (space between the planes of lattice points in the crystal lattice), and ϑ is the angle at which the electron approaches the crystal lattice planes. Incident electrons diffract through the sample and create two signals, a direct beam (incident beam electrons) and a diffracted beam. The beam used to form the image is selected with an aperture in the back focal plane. If the direct beam is chosen, one obtains a "bright field" image. Dark areas represent places where electrons have been diffracted away by defects etc, and create image contrast. Correspondingly, a "dark field" image uses the diffracted beam. High Resolution TEM (HRTEM), or phase contrast, images rely on the changing phases of electron waves due to interaction with the sample. This imaging mode can reveal crystallographic structures, such as single crystal defects and atoms. STEM images are produced raster scanning the focused electron beam over an area of the sample, much akin to a SEM.

3.4.3.2 *Experimental System*

A Jeol 2100F FEG transmission electron microscope (TEM), shown in figure 3.23, was used in this study under the direction of Dr. Budhika Mendis [41]. This system uses a Schottky field emitter operating at a voltage of 200 kV. The spatial resolution of this machine is 2.3 Å, great enough to pick out atomic detail in samples. The microscope has the ability to perform scanning transmission electron microscopy (STEM) imaging EDX and electron energy loss spectroscopy (EELS). EDX is very precise with this system as, in transmission electron microscopy, the interaction volume from the incident electron beam is very small, improving spatial resolution.

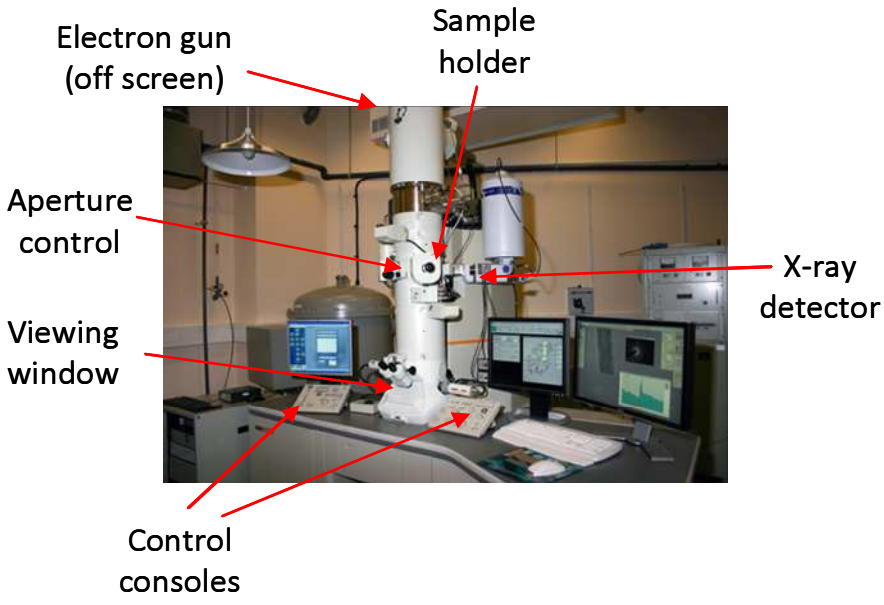

Figure 3. : An image of the Jeol 2100F FEG transmission electron microscope used in this investigation.

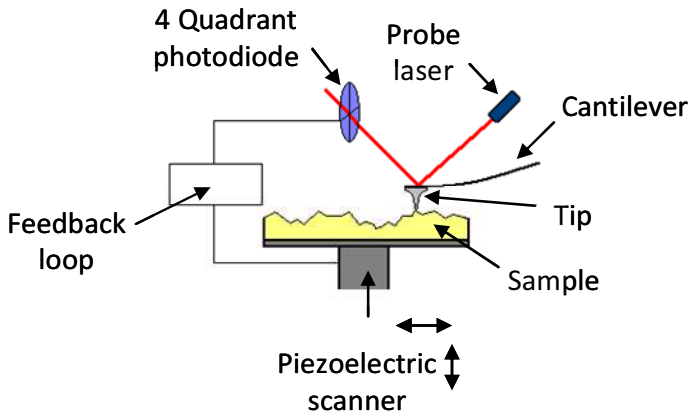

Figure 3. : Schematic diagram of the primary components of an atomic force microscope.

3.4.4 Atomic Force Microscopy

3.4.4.1 Principles

Atomic force microscopy (AFM) is an imaging technique that involves scanning an atomically sharp tip, located at the end of a cantilever, in very close proximity over a sample surface [46]. Forces (including van der waals, electrostatic forces etc) between the tip and surface cause deflection of the cantilever, obeying Hooke's law in equation 3.5. The deflection of the tip is measured using a laser beam, which is directed onto the back of the tip and is reflected to a quadrant photodiode. When the cantilever is displaced, the photodiodes collect differing amounts of laser light. This signal is proportional to the deflection of the tip, and so image contrast can be obtained. Figure 3.24 is a schematic diagram of an AFM. Either the sample or the AFM cantilever tip is attached to a piezoelectric scanner, which enables a constant force to be maintained between the tip and the sample, or for the cantilever to be kept at a constant height.

$$F = -kx \tag{3.5}$$

where *F* is Force, *k* is the spring constant and *x* is displacement/extension.

AFM has 3 imaging modes; contact, non-contact and tapping [46]. In contact mode, the cantilever tip is kept at a constant deflection (constant force between the tip and the surface) and scanned across the sample to form an image. However, forces can be very strong so close to the sample and there is a risk that the tip will contact the sample, potentially damaging both the sample and the tip itself. Non-contact mode avoids tip damage from sample collision, but produces images of lower resolution, particularly if the sample has developed an adsorbed fluid layer on its surface. In non-contact mode, the tip is oscillated at close it its resonant frequency. When close to the sample, interactive forces act to lower the resonant frequency of the tip. Changes in the amplitude and frequency of the oscillation of the tip can be calculated to form a surface image. Tapping mode, a combination of the above two methods, utilises a tip oscillating at close to its resonant frequency. Surface forces lower the amplitude of this oscillation. A computer attempts to keep the oscillation amplitude constant, so topology can be measured [46].

3.4.4.2 Experimental System

A Digital Instruments Nanoscope IV Scanning Probe Microscope was used in this investigation to map the topography of a 10 µm x 10 µm area of a printed pressure sensitive ink. The AFM was used in tapping mode. The system is capable of mapping areas (spatial x,y resolution) of 0.4 µm x 0.4 µm up to 200 µm x 200 µm in size and can resolve surface features on the order of tens of nanometers.

4. Results and Discussion

4.1 Introduction

This chapter details results of electrical and structural investigations undertaken during the course of this research. The chapter begins with a description of general electrical and structural properties common with all pressure sensitive inks scrutinised in the study. This is followed by data and discussions of results from investigations into the effects of ink storage time, storage temperature, over-blending and the addition of hyper-dispersants, all prior to printing. To conclude, improvements and directions for future research in this topic will be suggested.

4.2 Generalized Electrical Behaviour and Morphology of Pressure Sensitive Inks

4.2.1 Electrical Behaviour

Electrical transport measurements, recording the behaviour of sample current with varying voltage, were undertaken as described in section 3.3. All of the pressure sensitive ink samples, regardless of age, storage and blending conditions and with or without hyper-dispersant, display the same overall general form of electrical behaviour. The shape of the current-voltage plots was found to be dependent on compression. Figure 4.1 is an example of one cycle at a low compression (high resistance).

The current displays a quadratic dependence on both increasing and decreasing voltage. However, upon decreasing the voltage, the current is lower. There is also some hysteresis in the I-V behavior. Subsequent cycles show a similar pattern of “negative hysteresis”, as shown in figure 4.2. The magnitude of hysteresis, i.e. the area created by the current voltage cycle, decreases rapidly after the first cycle and converges to an approximate single value, shown in figure 4.3.

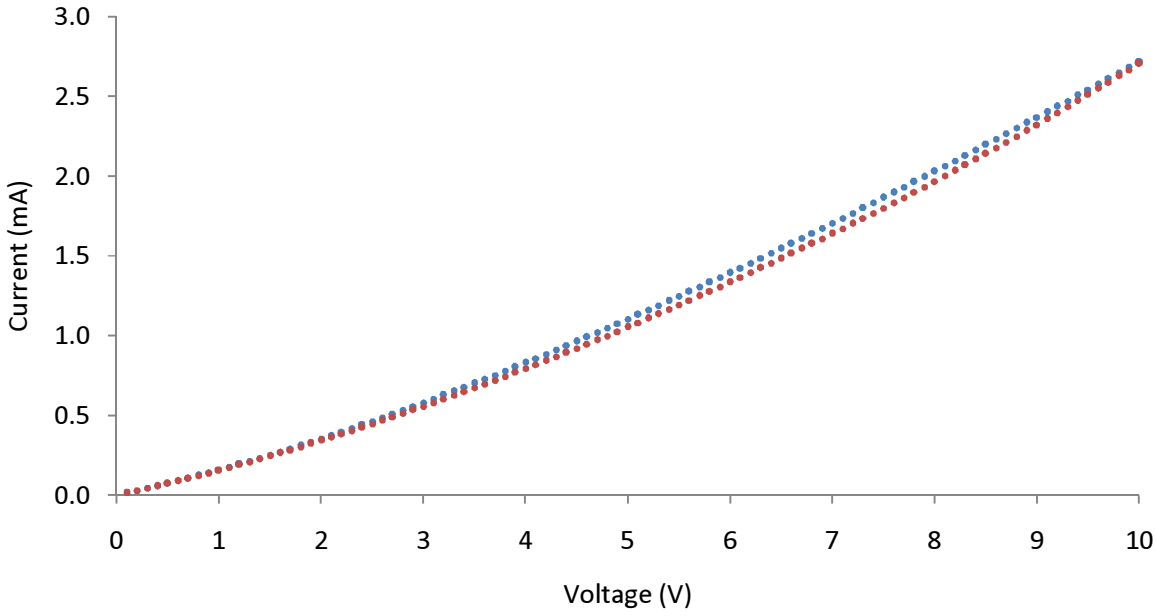

Figure 4. : First cycle of an I-V plot from an ink sensor compressed to 6.67 kΩ. The blue data points are the current measurements taken whilst ramping up the voltage to 10V, the red points are measurements of current taken when decreasing the voltage. The error bars are smaller than the data points.

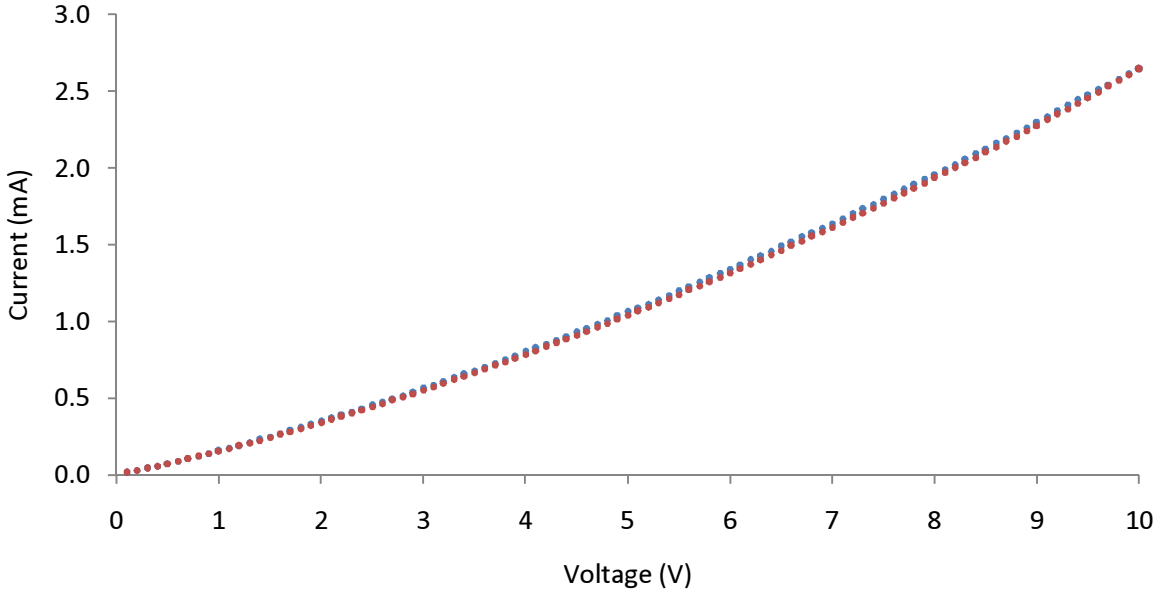

Figure 4. : Second cycle of an I-V plot from an ink sensor compressed to 6.67 kΩ. Blue data points are current measurements taken with increasing voltage, red points with decreasing voltage. The error bars are smaller than the data points.

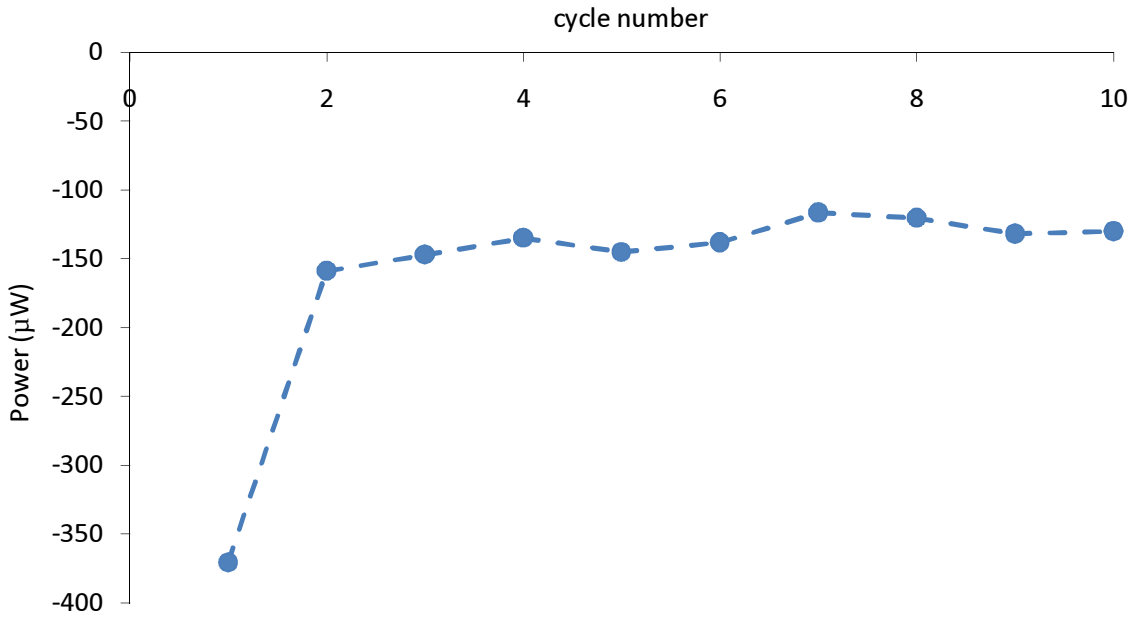

Figure 4. : Magnitude of hysteresis (Power) recorded for each I-V cycle from an ink sensor compressed to 6.67 kΩ. Error bars are smaller than the data points.

As the compression increases the average hysteresis becomes a larger negative value, and then switches to a positive value, shown in figure 4.4. Figure 4.4 also reveals an ink age sensitive process related to the hysteresis. The blue points are taken from a 2 day old ink, which displays the largest degree of hysteresis. Older inks, the red and green data points, exhibit less hysteresis overall. The negative hysteresis in the I-V curves from figures 4.1 and 4.2 appear to indicate the conductivity of pressure sensitive ink is lowered when the voltage is decreased on the down ramp of the voltage cycle (red data points). This may be a result of charge being trapped during the voltage increase and pinching off some of the routes through which electrical current can flow through the ink. The behaviour shown in figure 4.4 might be a result of age dependent partial separation/settling of components in the ink, forming distinct layers within the sensor. The conductive filler particles might separate from the insulating base ink, forming conductive and insulating layers.

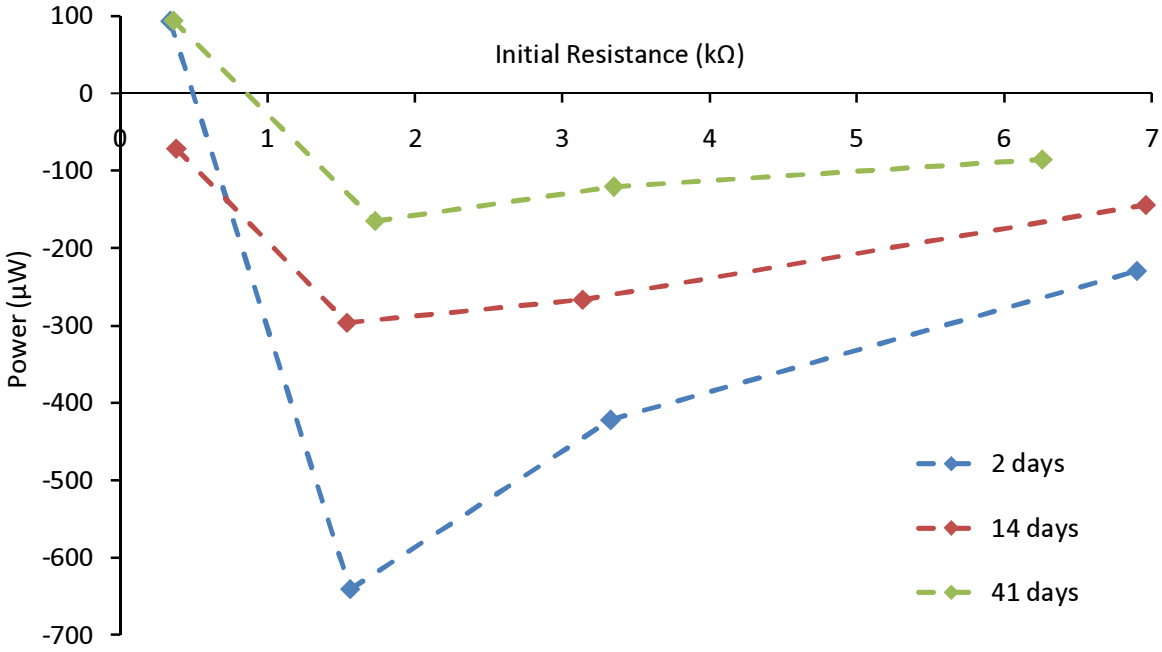

Figure 4. : Average hysteresis power as a function of resistance (compression) for 3 identical inks stored for 2 days (blue), 14 days (red) and 41 days (teal) before printing. The dashed lines are guides to the eye. Error bars are smaller than the data points.

If the conductive layer is more readily compressible, then as more force is applied to the ink sensor, the conductive layer will compress much faster than the insulating layer.

This could mean that charge would have to pass through a relatively thicker insulating region (potential barrier or region with the most charge trapping sites) with increasing compression. At a certain point, compression may be high enough to reduce the thickness of the insulating layer (making the potential barrier thinner), causing the hysteresis to switch to a positive value, seen in figure 4.4.

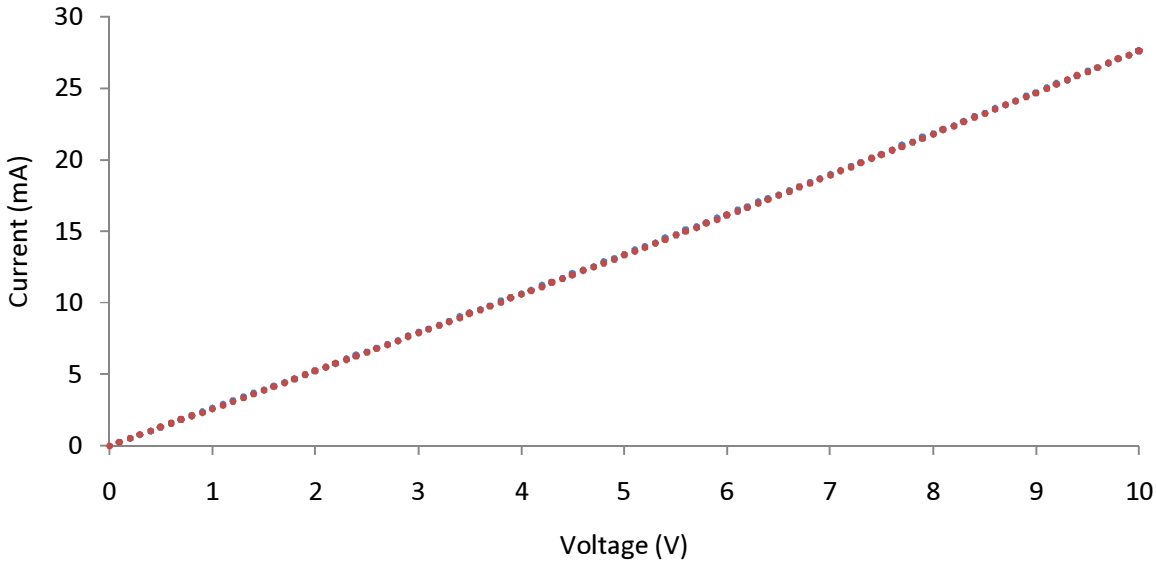

Figure 4. : First cycle of an I-V plot from an ink sensor compressed to 0.38 kΩ. Blue data points indicate current measurements taken when increasing the voltage, red points are current measurements taken when decreasing the voltage. The error bars are smaller than the data points.

Samples under a higher compression (lower initial resistance) exhibit current-voltage cycles that are more linear in appearance. At maximum compression, the behaviour is almost completely linear, shown in figure 4.5.

All of the current-voltage plots can be modeled well with quadratic and linear terms, which decrease and increase with increasing compression, respectively. Figure 4.6 shows the fits applied to an example I-V cycle. These fits of the data seem to closely match the behaviour predicted by the NLRRN and DRRN models described in section 2.6. Both models allow the current-voltage behaviour of a random resistor network to be described using equation 2.16, which is repeated below.

$$I = G_1 V + G_2 V^2$$
$$I = V\left(G_1 + G_2 V\right) \tag{2.16}$$

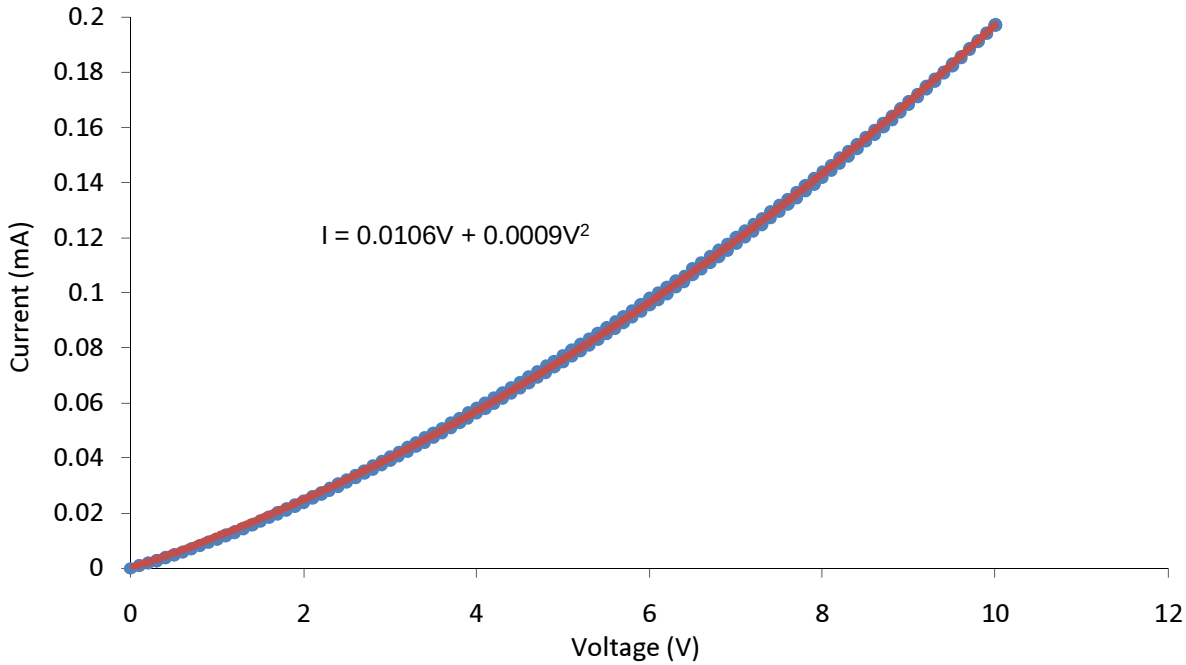

Figure 4. : Quadratic and linear term fit (red line) to an I-V cycle from an ink sensor compressed to 92.5 kΩ. The blue data points represent the current measurements. Error bars are smaller than the data points.

The coefficients G_1 and G_2 are the linear and non-linear coefficients, respectively. They actually represent electrical conductance (how easily electricity flows through electrical elements). *I* and *V* are the current and voltage. Equation 2.16 shows that, as the voltage is increased, non-linear behaviour becomes more pronounced. Applied to pressure sensitive inks, the value of G_2V is approximately ~10^{-2} smaller than the corresponding value of G_1. This means that, in the voltage range investigated here (0 to 10 V), the current is largely linear. The variance of the non-linear and linear conductance as a function of initial resistance is given below in figure 4.7 and figure 4.8, respectively. The non-linear component, G_2V, initially rises, but then drops at maximum compression. The linear conductance, G_1, rises rapidly with increasing compression. The temporary rise of the non-linear conductance may be a result of the relative thickness of conductive and insulating layers, mentioned previously.

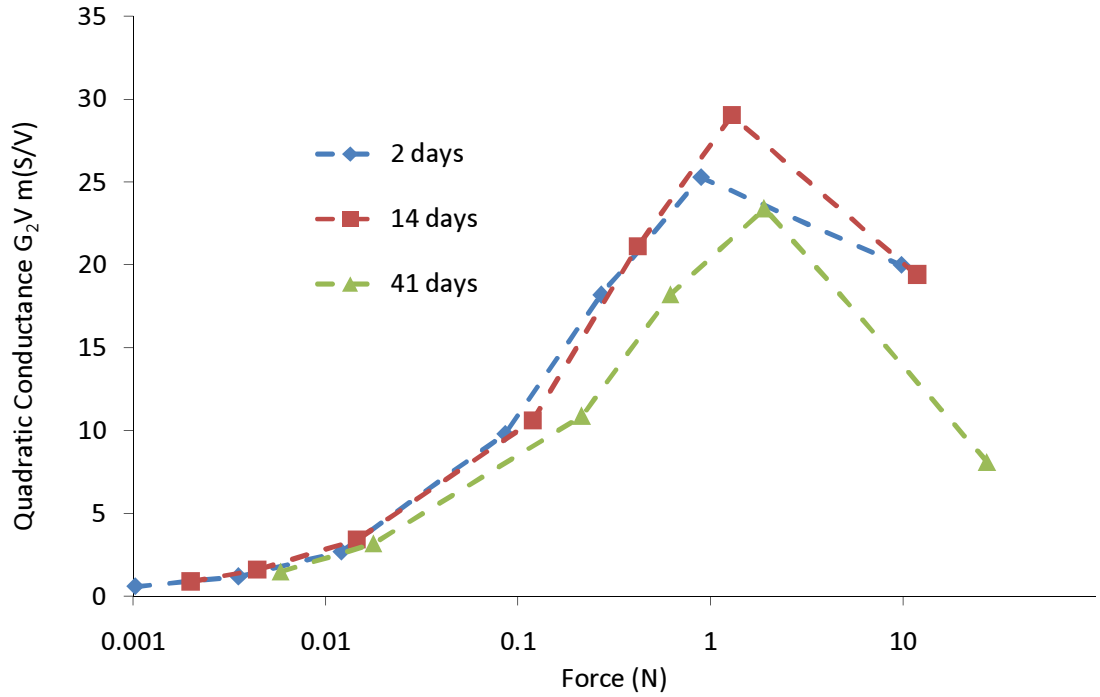

Figure 4. : Non-linear (quadratic) conductance variance with applied force (compression) and ink age. The dashed lines are guides to the eye. Error bars are smaller than the data points.

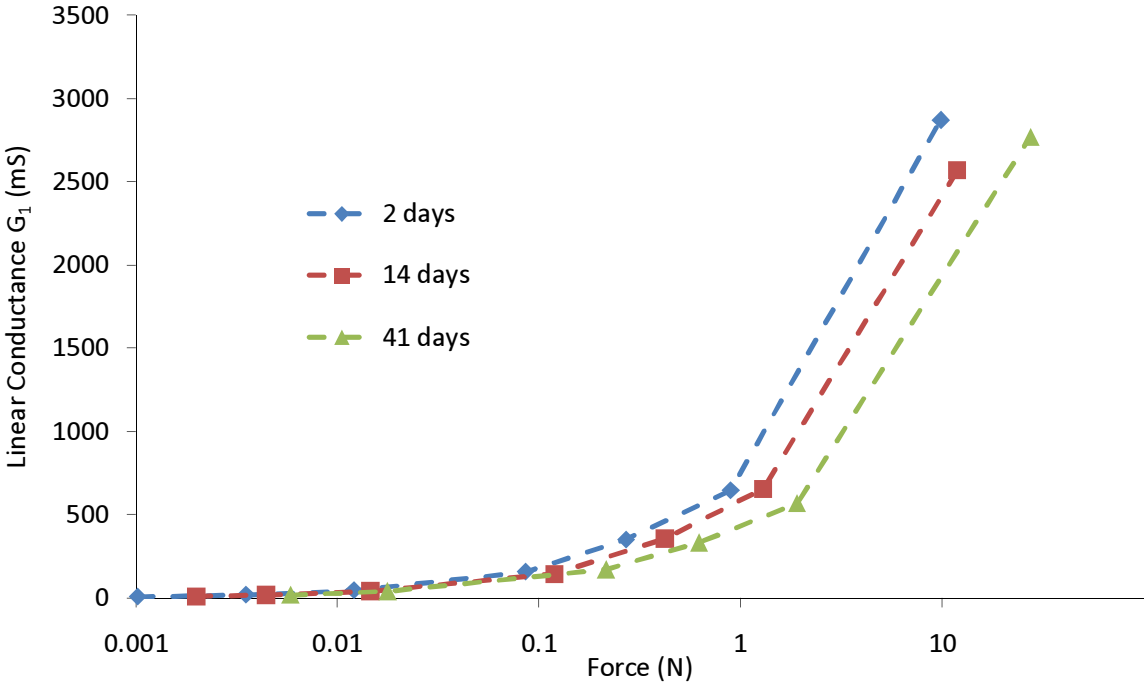

Figure 4. : Linear conductance variance with applied force (compression) and ink age. Dashed lines are guides to the eye. Error bars are smaller than the data points.

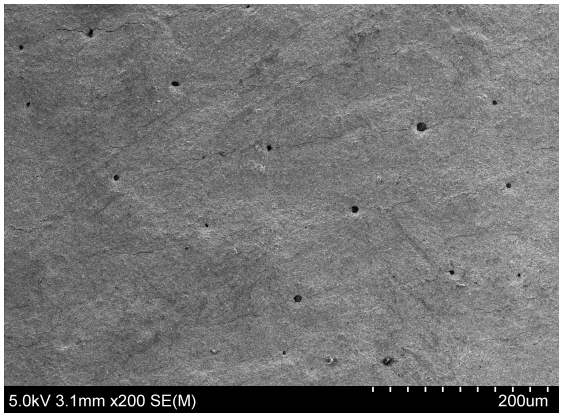

Figure 4. : A x2000 magnification SEM image of an ink sensor surface. The black spots are holes in the pressure sensitive ink layer caused by the screen printing mesh and air bubbles.

Alternatively, the variance of the linear and non-linear terms with resistance (compression) could be a result of changing conduction mechanisms. It is possible that, as compression is increased, filler particles get closer together and the degree of quantum tunneling processes increases, contributing to the rise of the non-linear conductance. At the same time, direct contact between filler particles would become more frequent. Eventually there might be a critical compression, which could exist at approximately close to 2N from looking at figures 4.7 and 4.8, at which many quantum tunneling connections between conductive filler particles become direct contacts, causing a drop in the non-linear conductance and a sharp rise in the linear conductance.

4.2.2 Morphology

All of the pressure sensitive inks have the same general appearance, all consisting of acicular (needle-like) particles dispersed in base ink. Figure 4.9 is a low magnification image of an ink sensor surface. The dark spots are the result of air bubbles, most likely created when the ink is mixed and blended, and printer defects, probably as a result of the ink being forced around the knuckles of the masked mesh during the screen printing process.

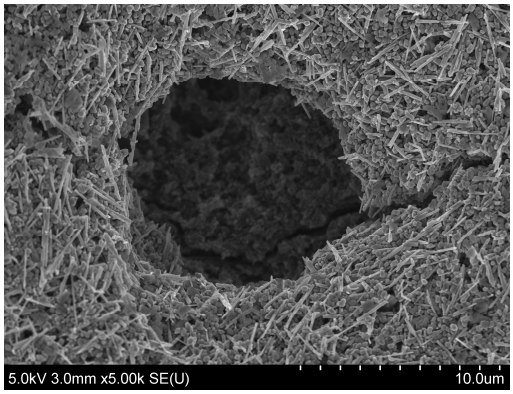

Figure 4. : A x5000 magnification SEM image of a single printing defect/air bubble. The defects/bubbles penetrate completely through the pressure sensitive ink layer and act as points of structural weakness, demonstrated by the crack in the ink surface which passes through the defect/bubble.

Figure 4.10 is a higher magnification of a single hole, which goes straight down to the carbon black layer underneath the ink. Zooming in, it is possible to see the individual constituents of the ink, shown in figure 4.11. The acicular particles, titanium dioxide nanorods, coated in a thin layer of conductive tin oxide (referred to as K2 particles from now), are dispersed in the base ink, which itself consists of titanium dioxide chunks, roughly spherical in shape, with an organic coating (to be referred to as TiOx particles).

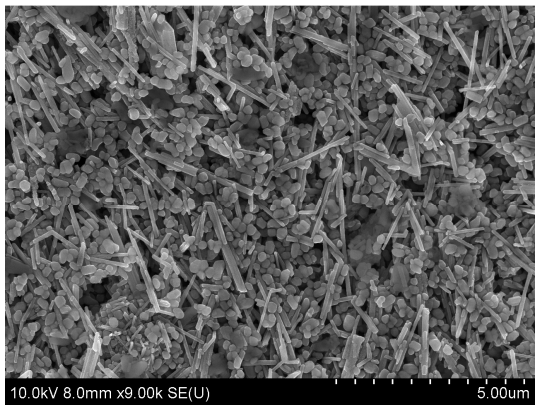

Figure 4. : A x9000 SEM image of an ink sensor surface. The electrically conductive nanorods and base ink material ("spherical" chunks) are clearly visible. Also, anomalous aggregates, darker in appearance, can be seen on the surface.

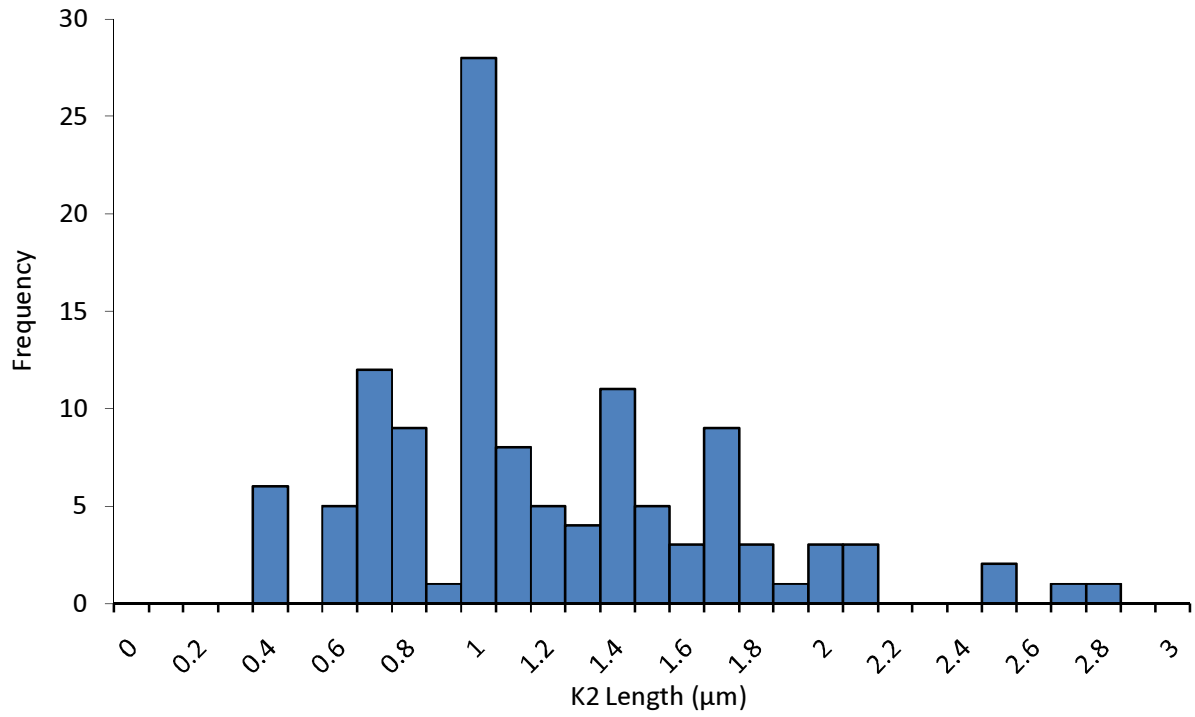

Figure 4. : A histogram of filler nanorod length, acquired from a survey of 120 nanorods. The distribution is not entirely Gaussian, with a tail to the longest nanorod lengths of ~3 µm. The shortest nanorods are ~0.4 µm long. Most of the nanorods have a length of ~1 to 1.2 µm.

Although quite well dispersed, the K2 particles tend to clump together in groups of 3 or more. Across the surface, dark aggregates have formed. These aggregates are anomalous and investigated in the following section. There also appear to be small gaps in the surface. A survey of 120 filler K2 and 120 TiOx particle dimensions gave the average width and length of filler K2 particles to be (87 ± 1) nm and (1.20 ± 0.05) µm respectively, and the width of TiOx particles as (202 ± 1) nm. A histogram of filler K2 length is given in figure 4.12. Analysis of an ink sensor sample with AFM gave an RMS roughness of 300 nm, with a peak height of 2133 nm (the lowest height was defined as zero) [47]. Due to the rough surface, the AFM was not used to obtain ultra high resolution images of the surface, as the tip could have easily been damaged. Figure 4.13 is a three dimensional image of the surface as generated by the AFM data [47].

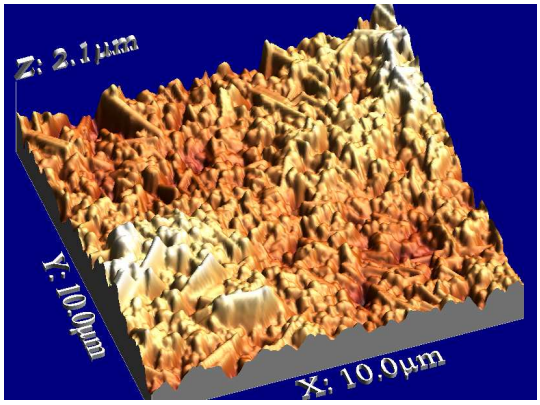

Figure 4. : A three dimensional image of a pressure sensitive ink surface rendered from AFM data.

Figure 4.14(a) is a high resolution image of some K2 particles. The surfaces of the K2 particles are covered in small nodules. This feature is investigated in section 4.3. Figure 4.14(b) is an image of some TiOx particles. These particles are all covered in a stringy substance, presumably the organic coating from the ink. Figure 4.15 is a cross section image from a well which was FIB milled in the surface of a sensor. There are 3 distinct layers in the cross section. The bottom, dark layer is carbon black, the contact pad material printed beneath the pressure sensitive ink. From this image, it appears K2 and TiOx particle segregation has occurred after the blending stage.

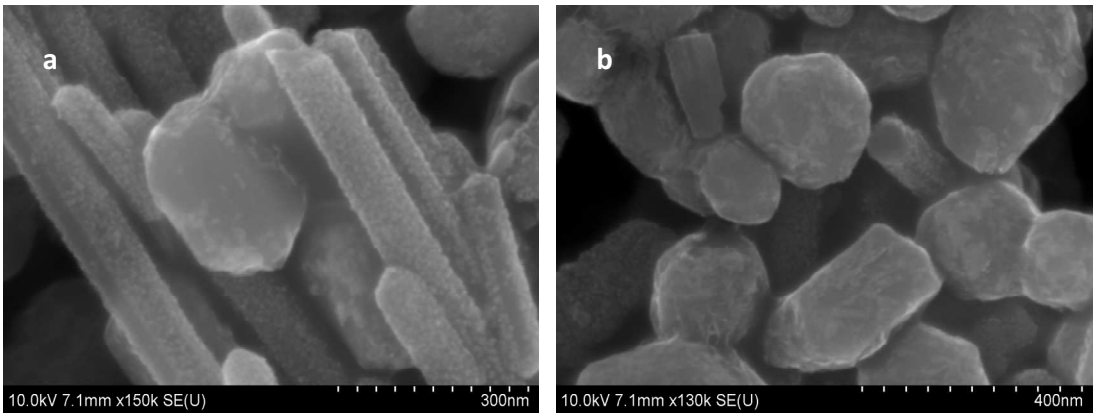

Figure 4. : (a) x150 000 magnification SEM image of conductive filler nanorods. The surfaces of the nanorods appear rough, coated in nanoscale nodules. (b) x130 000 magnification SEM image of base ink particles. The particles have patchy, stringy surface features, which may be an organic coating.

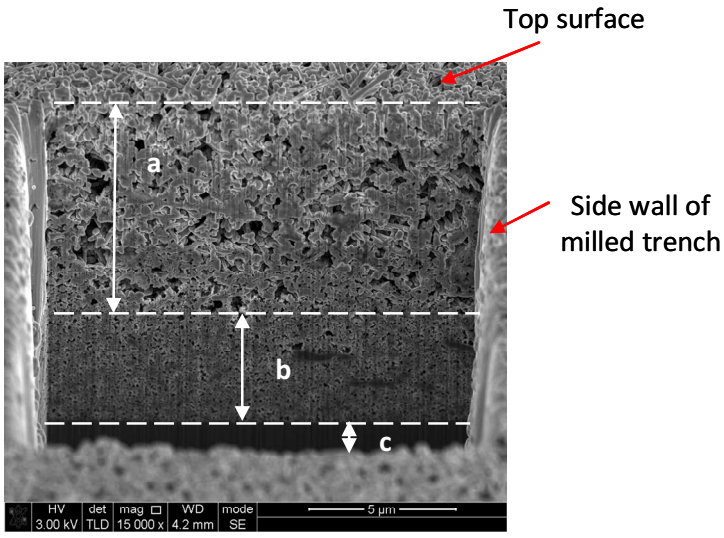

Figure 4. : A FIB well etched into the surface of an ink sample. The top layer, containing most of the K2 particles, is labelled (a). The more compact TiOx particle layer is labelled (b). The bottom carbon black layer is (c). It should be noted that the sample is tilted 52° to the horizontal.

The top layer contains most of the electrically conductive K2 particles, which all seem to lie flat, in the horizontal plane of the sensor. The ink also is less compact in this region, with many gaps in the ink present. Below this area, the ink transitions into a more compact region, containing predominantly what appear to be smaller TiOx particles. This evidence of segregation is further scrutinised in the following section.

4.3 Investigation of Ink Storage Time

4.3.1 Introduction

Referring back to figure 3.1, inks are made by mixing basic constituents, undergoing a blending process and being stored before finally being printed. This investigation looks at stage 3 of this procedure, the storage stage. Blended inks are poured into pots and left to stand until they are needed for printing. Inks that have been left to stand for a very short time, 2 days, for example, perform well and are highly sensitive to touch pressure. Inks stored for longer periods of time,

ranging from weeks to more than a month, begin to show decreased sensitivity. The electrical behaviour and morphology of such inks is detailed below.

4.3.2 Electrical Behaviour

Inks left to stand for longer periods of time lose pressure sensitivity, best depicted in figure 4.16, which shows how the conductivity of pressure sensitive ink varies with increasing applied force. All of these sensors were produced from the same blend, i.e. printed from ink stored in a single pot. The sensors were, however, printed after leaving the ink to stand for increasing amounts of time. The youngest sensor in the set is made from 2 day old ink, the oldest sensor is made from 41 day old ink.

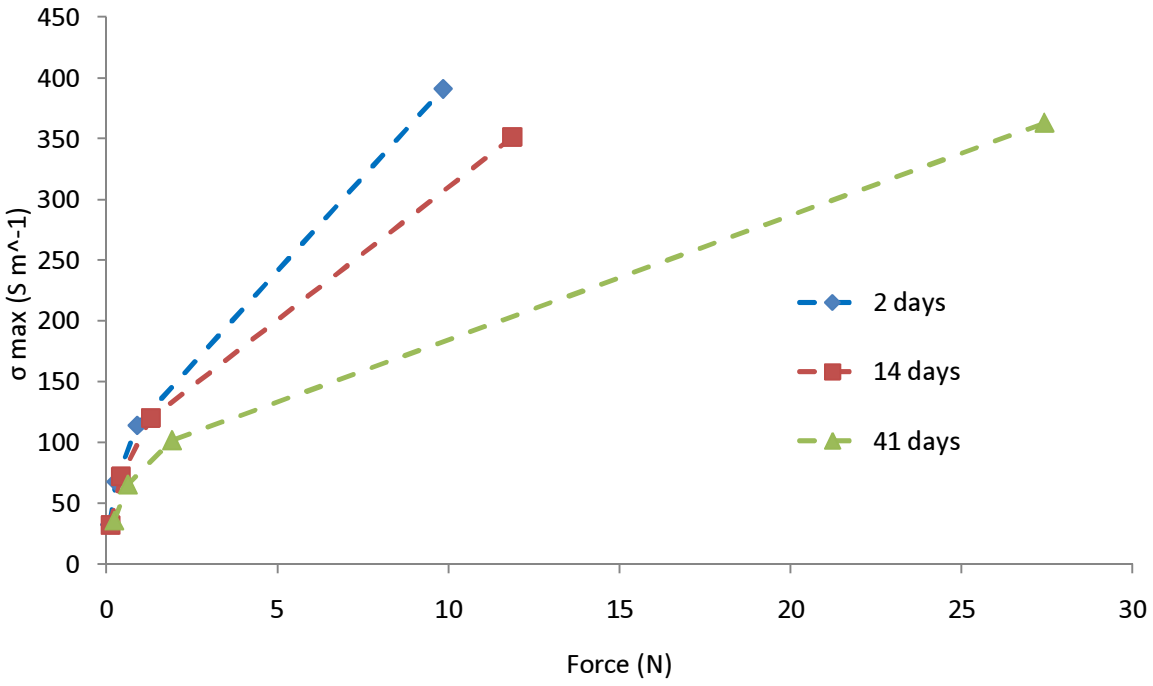

Figure 4. : Conductivity behaviour with respect to increasing applied unilateral force. The blue data points were taken from a 2 day old sample, red points from a 14 day old sample and green points from a 41 day old sample of ink. The dashed lines are a guide to the eye. Error bars are smaller than the data points.

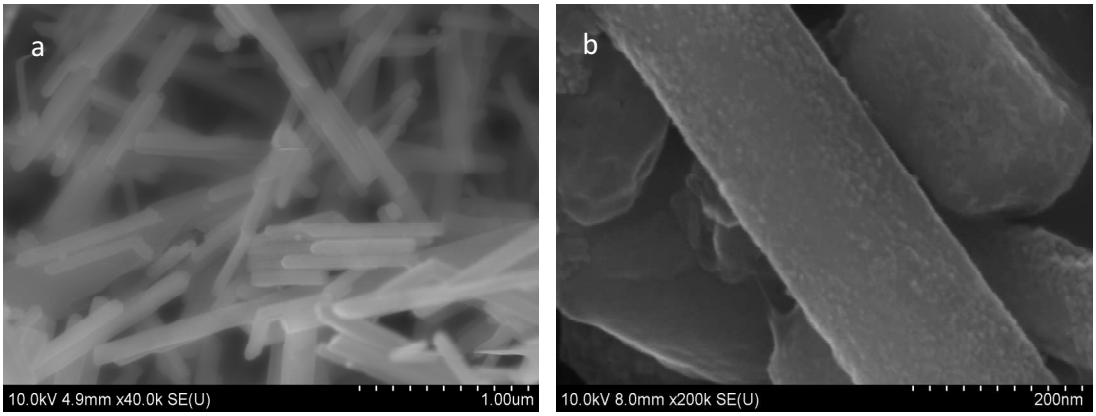

Figure 4. : (a) x40 000 magnification SEM image of K2 particles prior to mixing with base ink. The particles are noticeably smoother. (b) x200 000 magnification SEM image of a K2 particle in an ink aged for 2 days prior to printing. Nanoscale features can be seen on the K2 surface.

4.3.3 Morphology

At first glance, it may appear that the ink constituents do not change with increasing storage time. However, close scrutiny of the K2 particles reveals they develop surface features with age, once mixed and blended with the base ink. Figure 4.17(a) is an SEM image of some K2 particles before being mixed with the base ink. The needles, for the most part, are very smooth. Comparing this to figure 4.17(b), it is clear that the K2 particles acquire nanoscale surface features after just 2 days of storage when mixed with the base ink. These surface features or nodules seem to increase in density with increasing age, as figures 4.18(a) and 4.18(b) demonstrate, which are images of K2 particles in 14 and 41 day old inks, respectively. However, it should be noted that it was not possible to quantify the growing thickness of the nodules.

Figures 4.19(a) and 4.19(b) are ultra high resolution images of the nodules from an SEM and TEM, respectively. The images show that the nodules are small crystallites of size 5 to 10 nm, on average.

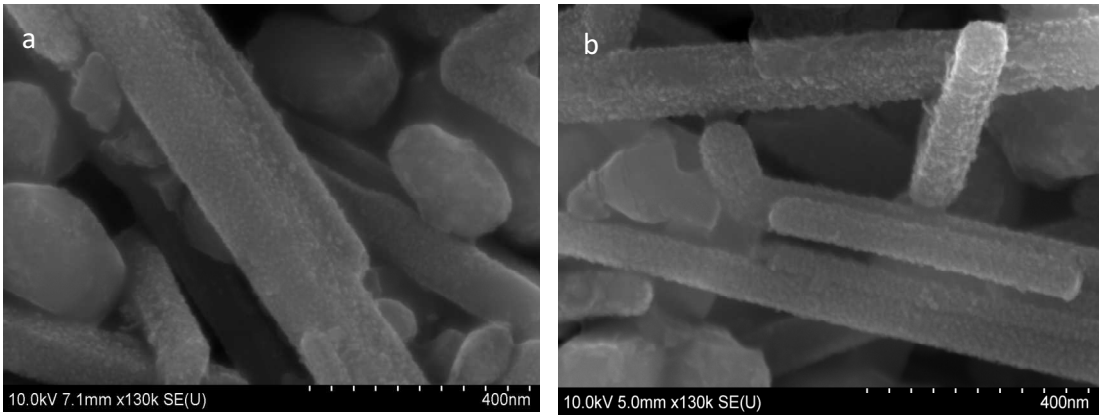

Figure 4. : (a) K2 particles in an ink stored for 14 days prior to printing. (b) K2 Particles in an ink stored for 41 days prior to printing.

The growth of surface features on the K2 particles correlates with the inks' decreasing pressure sensitivity with increasing age, and so may be a factor in determining the electrical conductivity of the inks. The nodules may do this by reducing the number of direct contacts between K2 particles and then, as the nodules grow in thickness, reduce the effectiveness of quantum tunnelling mechanisms.

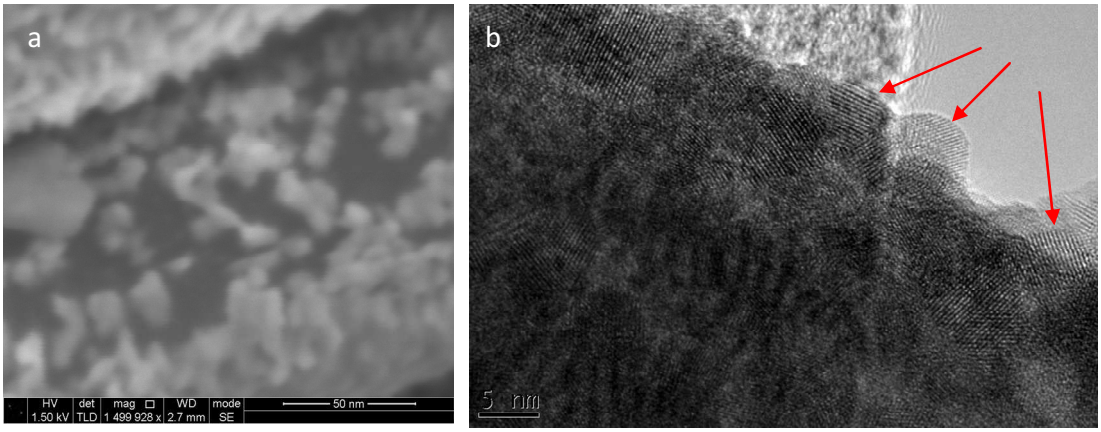

Figure 4. : (a) x1.5 million magnification SEM image of a K2 particle surface from a 41 day old ink. The nodules on the surface are ~5 to 10 nm in width. (b) Ultra high resolution TEM image of a single K2 particle taken from a 41 day old ink. The red arrows indicate nodules which can be more clearly seen. The TEM shows the nodules are nanoscale crystallite structures.

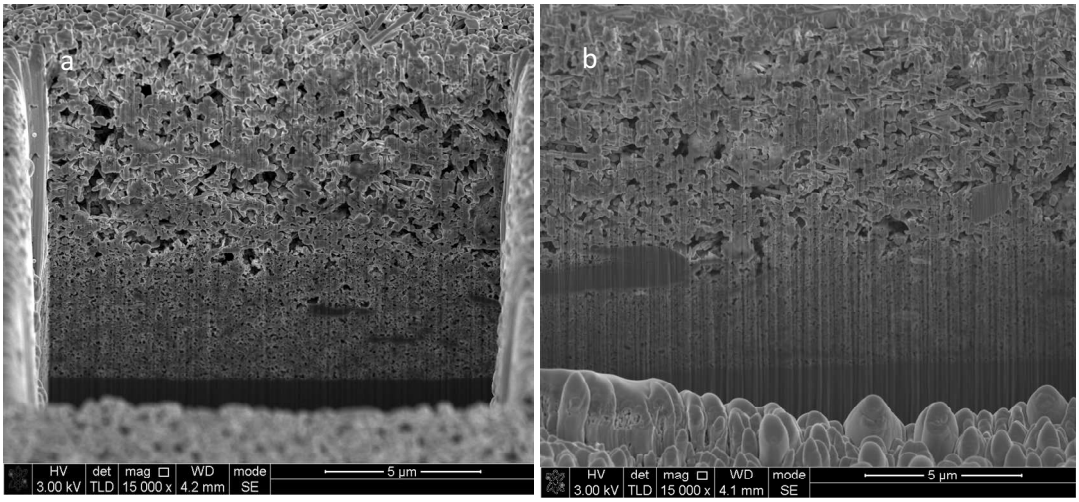

Figure 4. : (a) FIB milled trench in the surface of a 2 day old ink sensor. (b) FIB milled trench in the surface of a 41 day old ink sensor. Both SEM images were taken with the samples tilted at 52° to the horizontal.

Figures 4.20(a) and 4.20(b) compare two wells milled into ink sensors of 2 and 41 days of age. Both wells exhibit the same 3 regions; a bottommost layer of carbon black, a very compact layer comprising of what appears to be mainly small TiOx particles, and then a topmost layer of K2 and TiOx particles. The layers of small TiOx particles appear to be of roughly the same depth. There is a difference, however, in the upper layers containing the majority of the K2 particles.

The younger, 2 day old ink has a top layer which is far less compact than that of the 41 day old ink. This suggests that the segregation of particles is a relatively quick process, but that the K2 layer initially contains more air pockets and gaps, which close up and disappear as the ink ages. Older inks, with more compact regions, may then exhibit smaller hysteresis magnitudes as the relative thicknesses of the conducting and insulating layers are reduced.

4.3.4 Elemental Analysis

Energy dispersive analysis of X-rays (EDX) was utilised in both the SEM and TEM in order to identify the elements present in the inks, and specifically, the amorphous aggregates and K2 surface nodules. Figure 4.21(a) is an image the surface of an ink sensor, and figures 4.21(b) and 4.21(c) are spectra acquired from the locations marked on figure 4.21(a). Both spectra have the same overall features, showing signals of titanium, oxygen, carbon and tin, with a background signal of calcium causing broadening of the second tin L line, marked with an arrow.

Figure 4.22(a) is another image of an ink surface, this time including an aforementioned anomalous aggregate. The spectrum acquired from the aggregate, given in figure 4.22(b), shows a strong calcium signal. This is compared to a spectrum from a point away from the aggregate in figure 4.22(c), which is much like the spectra given in figures 4.21(b) and 4.21(c). It is highly likely, then, that the aggregates are comprised mainly of a calcium compound. Whether these aggregates are actually thick coatings around TiOx particles cannot be ascertained, however.

The identification of these aggregates led to a more detailed analysis of the K2 surface nodules. Using a TEM, element maps were obtained from a single K2 needle removed from a 41 day old ink. Figure 4.23(a) is the dark field image of the needle in question.

Figures 4.23(b), (c) and (d) show the element maps for titanium, tin and calcium respectively. The element maps identify the presence of calcium on the surface of the K2 particles, along with the tin.

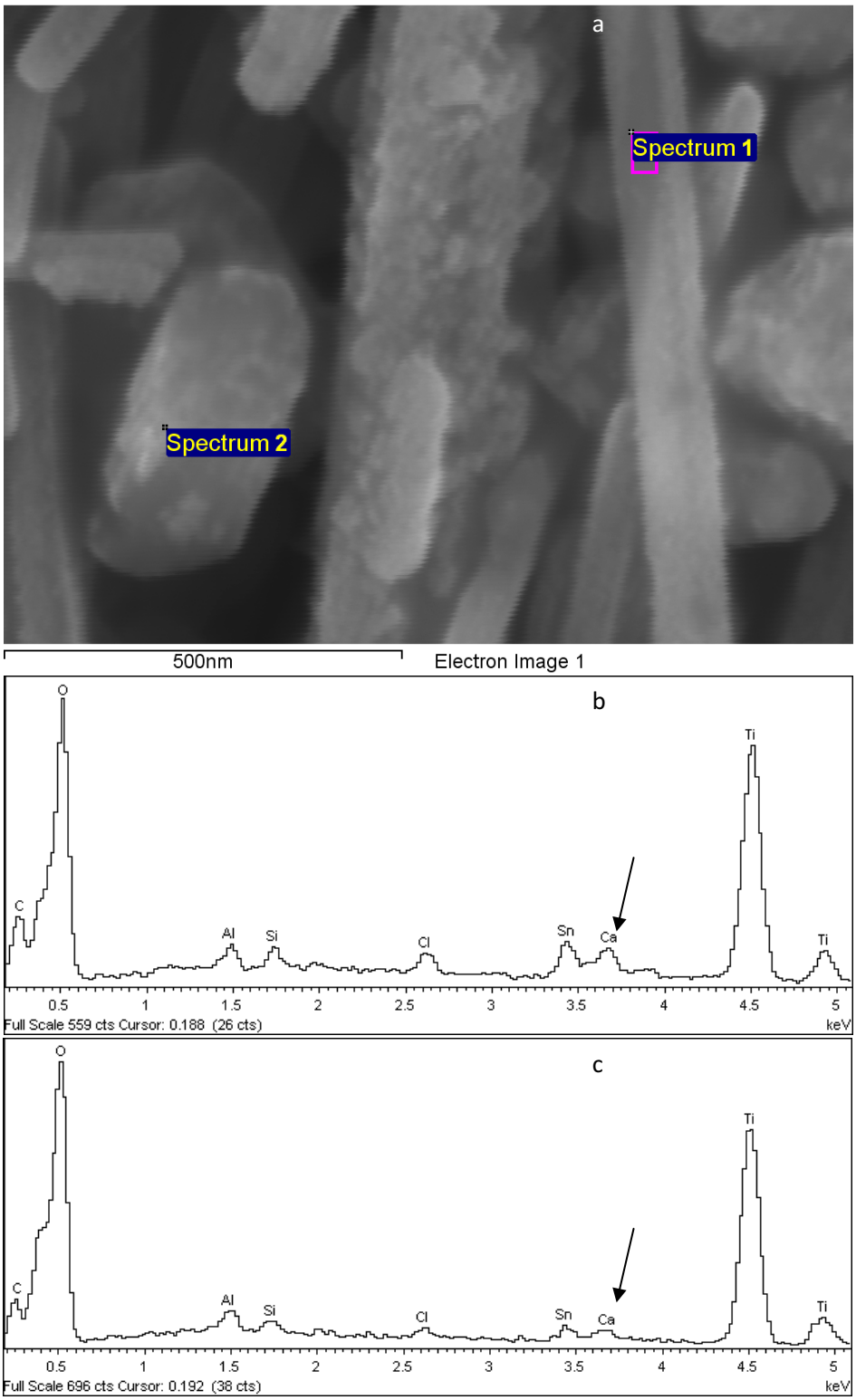

Figure 4. : (a) SEM image of ink sensor surface with spectrum locations. (b) Spectrum 1 from a K2 particle. (c) Spectrum 2 from a TiOx particle.

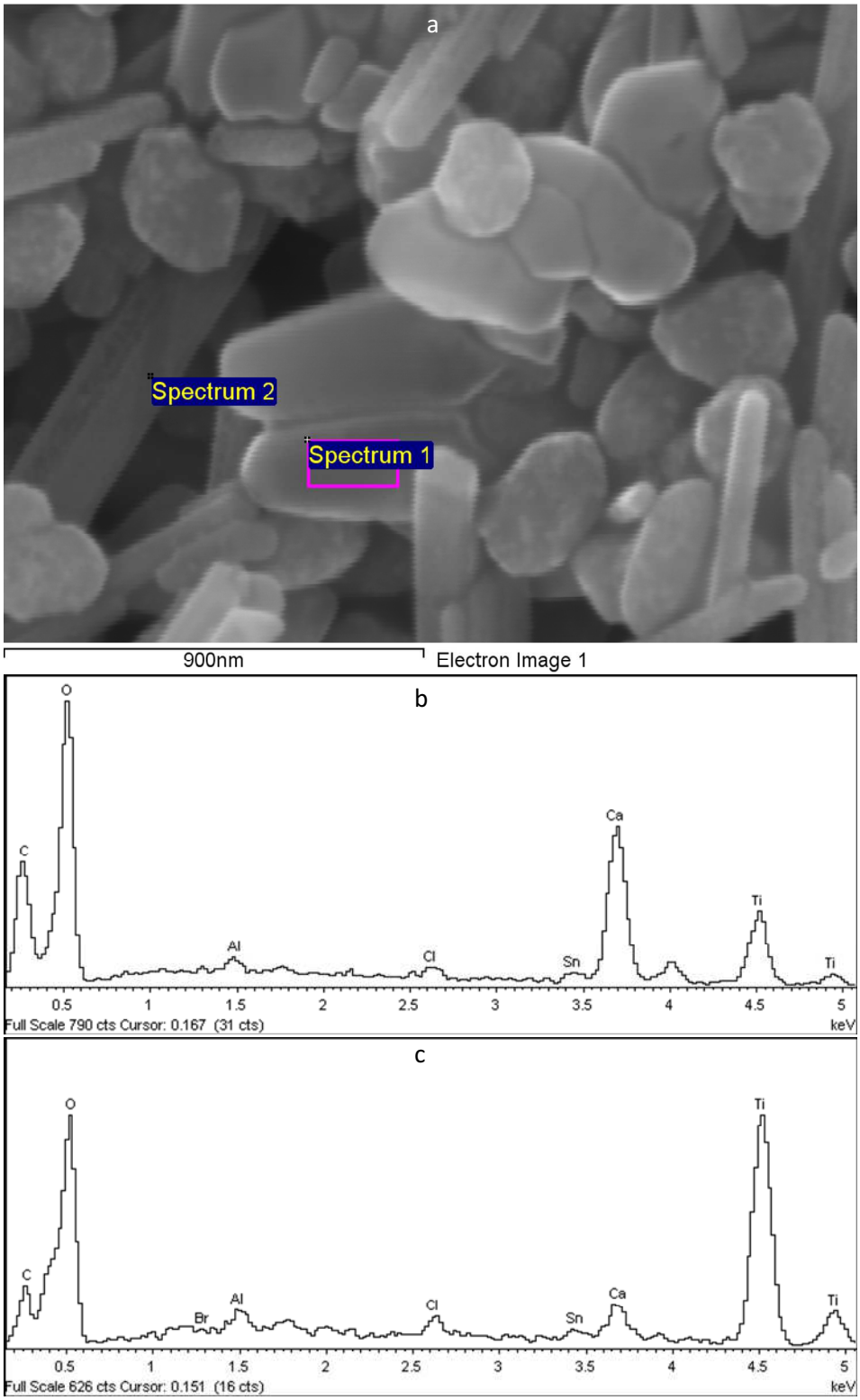

Figure 4. : (a) SEM image of ink surface with spectrum locations. (b) Spectrum 1 from anomalous aggregate. (c) Spectrum 2 from a separate area.

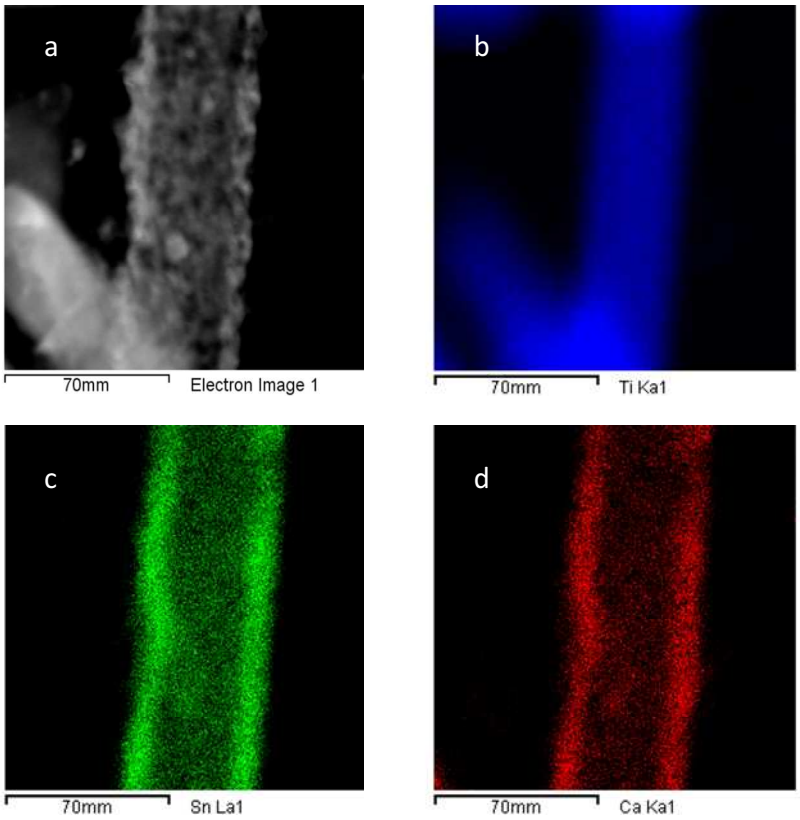

Figure 4. : (a) TEM dark field image of a K2 particle. (b) Titanium element map. (c) Tin element map. (d) Calcium element map confirms the presence of calcium on the surface of the K2 particle.

4.4 Investigation of Ink Storage Temperature

4.4.1 Introduction

This investigation also focuses on stage 3 of the manufacturing process outlined in figure 3.1. A batch of ink was produced and separated into two pots. One pot was stored under regular conditions, at room temperature. The other was kept refrigerated at 4°C. After a storage time of 58 days, both inks were printed as functional pressure sensors. The sensors made from the refrigerated ink were more sensitive than those made from the ink stored at room temperature. The electrical behaviour and structural analysis of these two inks is provided below.

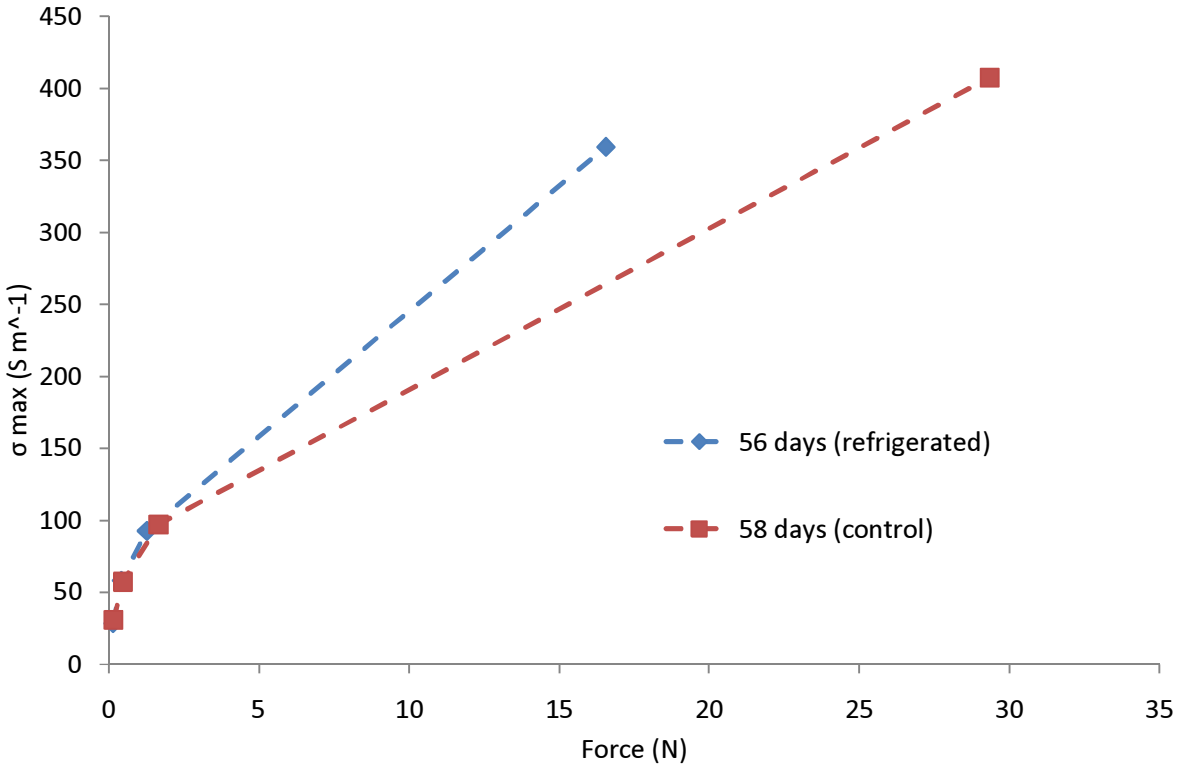

Figure 4. : Conductivity behaviour with respect to increasing applied force for an ink stored in a refrigerator at 4° (blue) and a control ink sample stored at room temperature (red). The dashed lines are guides to the eye. Error bars are smaller than the data points.

4.4.2 Electrical Behaviour

Refrigerated inks appear to retain greater pressure sensitivity over longer periods of time, behaving much like younger inks and exhibiting a greater decrease of resistance with applied force than those inks stored at room temperature for the same time.

Analysis of current-voltage plots, in particular the conductivity of the inks in figure 4.24, also supports this. The refrigerated ink retains a greater degree of pressure sensitivity and thus achieves higher conductivities from lower applied unilateral force. The difference in electrical behaviour implies a temperature dependent process effecting pressure sensitivity.

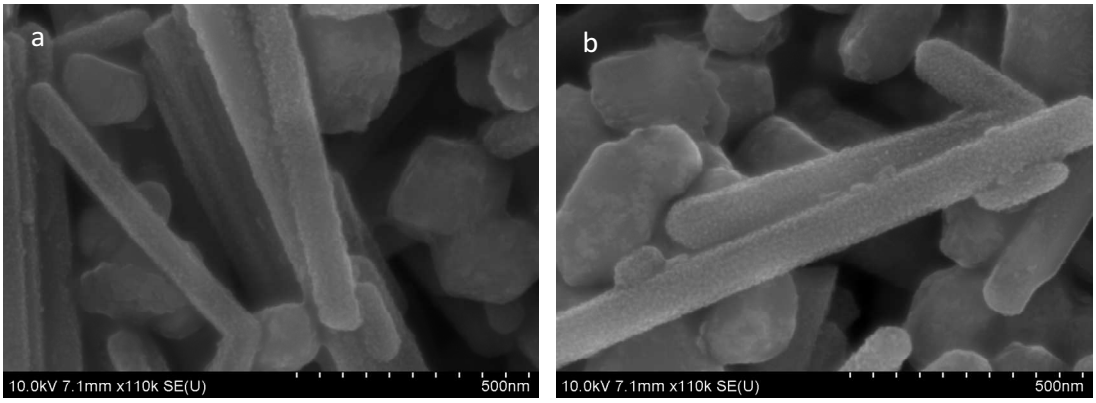

Figure 4. : (a) x110 000 magnification SEM image of K2 particles in an ink stored at room temperature for 56 days. (b) x110 000 magnification SEM image of K2 particles in an ink refrigerated at 4° for 58 days.

However, the refrigerated ink hysteresis behaviour is shifted to larger negative values than that of the control sample. This same shift is seen in the inks used for the storage time investigation, with younger inks generating more negative hysteresis.

4.4.3 Morphology

The electrical transport measurements suggested that an exothermic process is involved in the degradation of the inks' sensitivity to touch pressure. Figure 4.25(a) is an SEM image of the surface of the ink stored at room temperature. The K2 surfaces in figure 4.25(a) look very much like those found in the 41 day old ink from the storage time investigation. As the nodules on the K2 particles grow after the K2 particles have been mixed into the ink, it was expected that the refrigerated ink would contain K2 particles that are considerably smoother than the inks stored at room temperature.

However, as figure 4.25(b) demonstrates, this may not be the case. The ink surfaces of the refrigerated and room temperature samples are practically identical, with no discernable differences in K2 surface nodules to be seen.

4.5 Investigation of the Effects of Over-Blending Inks

4.5.1 Introduction

This section of the thesis concerns stage 2 of the manufacturing process detailed in figure 3.1. All pressure sensitive inks, after being hand mixed, are injected into a bead mill at a rate of 0.7 ml/s, and blended with the bead mill operating at 3000 rpm. For this investigation, ink was prepared and "over-blended" by altering stage 2. The ink was injected through the bead mill at a slower rate of 0.15 ml/s and the mill itself was run at 4000 rpm, providing a much more vigorous blending regime. The behaviour of the samples and their morphologies are compared below.

4.5.2 Electrical Behaviour

By analysing how ink sample resistance drops with increasing applied force, it can be shown that over-blended samples are less sensitive then those produced under standard guidelines. Over-blended inks behave as if they were older, requiring comparatively more applied force to achieve the same drop in resistance as a regularly blended ink. Conductivity measurements show over-blended inks performing as old inks do, with a poorer increase of conductivity, in figure 4.26.

4.5.3 Morphology

As mentioned in section 1.3 and previous research, over-blending nickel particles used in quantum tunnelling composites led to the loss of the sharp nickel spikes responsible for the materials electrical behaviour. It was thought that over-blending might have a similar effect on pressure sensitive ink, in particular on the K2 particles. In order to test this theory, a survey of K2 widths and lengths in over-blended inks was undertaken. Random K2 particles were measured across the entire surface of the samples, (a total area of $\{19.6 \pm 0.5\}$ mm^2).

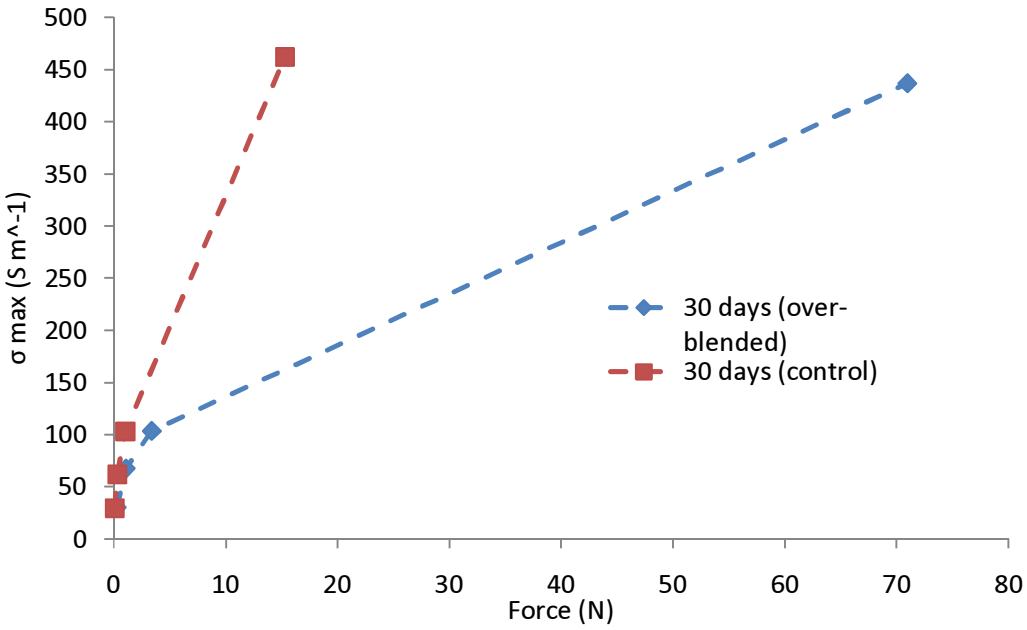

Figure 4. : Conductivity response to applied force from a regular sample (red) and from an ink sample which had been more vigorously blended (blue). The dashed lines are guides to the eye. Error bars are smaller than the data points.

The results of this survey were compared to the K2 dimensions measured in standard inks and are presented here. The widths of K2 particles that had been exposed to over-blending did not differ significantly from those blended under regular conditions. However, over-blending was found to dramatically alter K2 particle lengths. Figure 4.27(b) is a histogram of K2 lengths measured in a sample that was over-blended. Compared to figure 4.27(a), a histogram of K2 lengths in standard ink (repeated here from earlier in the investigation for easier viewing), it is evident that over-blending skews the distribution of K2 length to shorter lengths and generally flattens the distribution, eliminating the occurrence of many needles being the same length. The average K2 length in the over-blended sample is reduced to (0.90 ± 0.05) µm. Having shorter needles in the pressure sensitive ink will be detrimental to conduction if thought about in a percolation model. The shorter K2 needles will not be in contact as much, and may not come into contact as often when compressed, resulting in poorer conduction pathways across the ink.

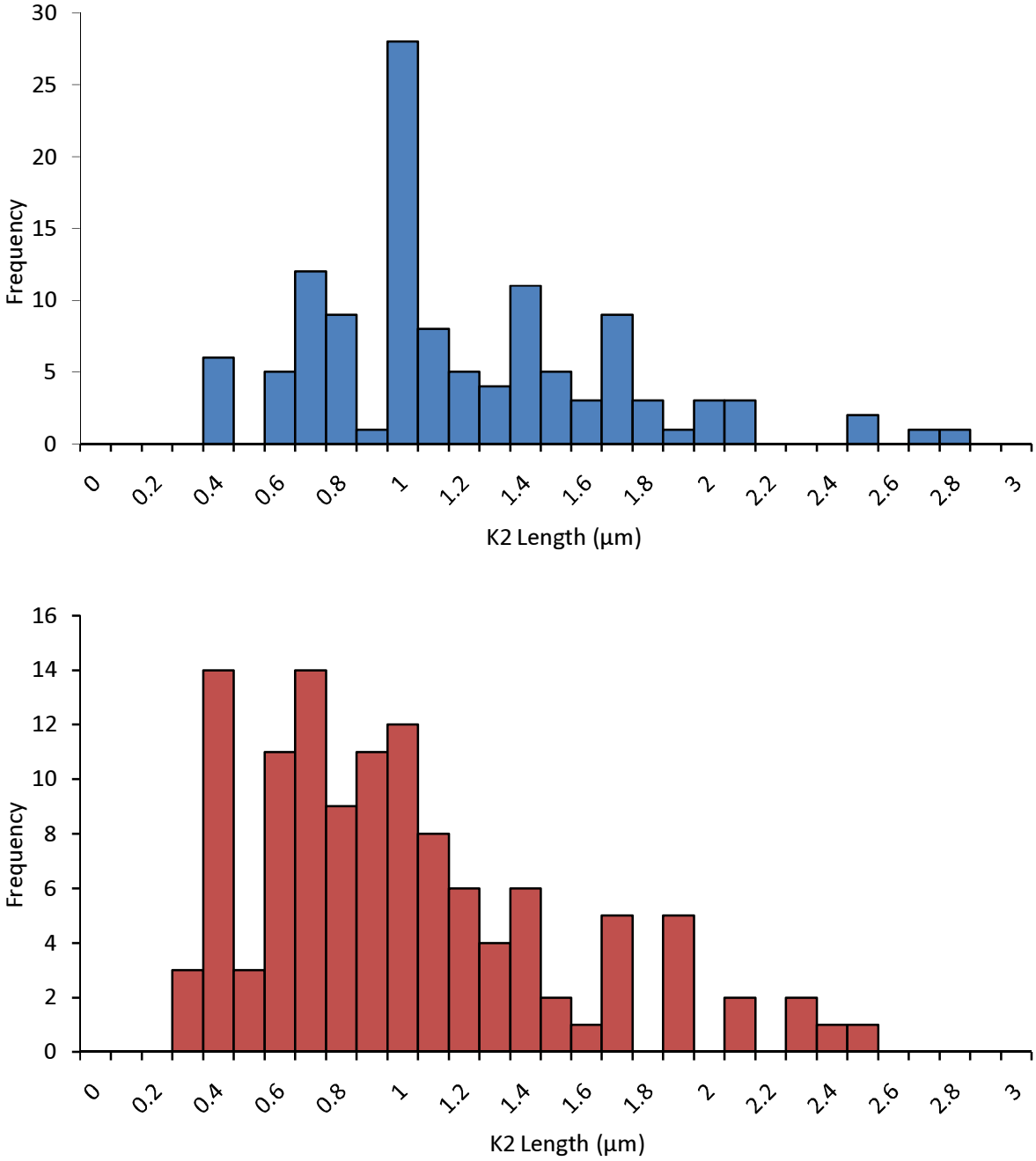

Figure 4. : (a) Histogram of K2 lengths from an ink mixed and blended according to regular guidelines. The distribution is not entirely gaussian, with a tail to longest lengths of ~3 µm. Most of the K2 particles are ~1.2 µm long. (b) Histogram of K2 lengths from an ink that has been more vigorously blended. Over-blending skews and widens the distribution to shorter lengths, and reduced the tail of lengths of ~2.6 µm. Shorter K2 particles become more common, with most having a length of ~0.9 µm. Both histograms were produced from surveys of 120 K2 particles each using SEM imaging.

4.6 Investigation of the Effects of Hyper-Dispersant

4.6.1 Introduction

This final investigation focuses on the effect the addition of hyper-dispersant (HD hereon after) has on pressure sensitive ink properties. HD is an anti-clumping agent and acts to prevent particles from aggregating, thereby lowering ink viscosity. In stage one of the manufacturing process in figure 3.1, if less K2 particles have been mixed in with the base ink, the final printed pressure sensitive ink does not function as well as those made with more K2 needles. The addition of HD to these inks with less K2, however, improves their performance dramatically so that they are almost as sensitive as regular inks. The following two sub-sections look at this effect and detail the results of the investigation.

4.6.2 Electrical Behaviour

Inks produced with less K2 particles relative to base ink are less sensitive to touch pressure than regular inks. Inks with lower K2 fractions require more force to lower resistance to the same degree as regular inks and so are analogous in behaviour as old, normal K2 fraction inks. Their properties degrade with age in the same fashion, however. The magnitude of hysteresis of low K2 fraction inks is far less than that of regular inks. When HD is added to low K2 fraction inks, however, their electrical behaviour emulates standard inks and their sensitivity to pressure in increased. The effect of HD can also be seen in a graph of force against sample resistance, figure 4.28, which compares the conductivity response to force of a sample with and without added HD.

4.6.3 Morphology

Low K2 fraction inks have noticeably less K2 needles on their surface compared to regular inks. This, combined with the fact that the K2 particles have a tendency to clump together may lower the probability that a conduction pathway will form as the force increases, reducing the sensitivity to

pressure. Figure 4.29(a) is an SEM image of a low K2 fraction ink surface and is compared to figure 4.29(b), an SEM image of a low K2 fraction ink surface with added HD. The addition of HD should break up many of the K2 clumps and allow better dispersion of the K2 particles. This was tested by recording the density of K2 needle clumps in low K2 fraction inks and in inks with added HD.

A clump was defined as a group of 3 or more needles bound together for the purpose of the test. The result gave a clump density of (0.17 ± 0.01) μm^{-2} in low K2 fraction inks and a density of (0.09 ± 0.01) μm^{-2} in inks with added HD.

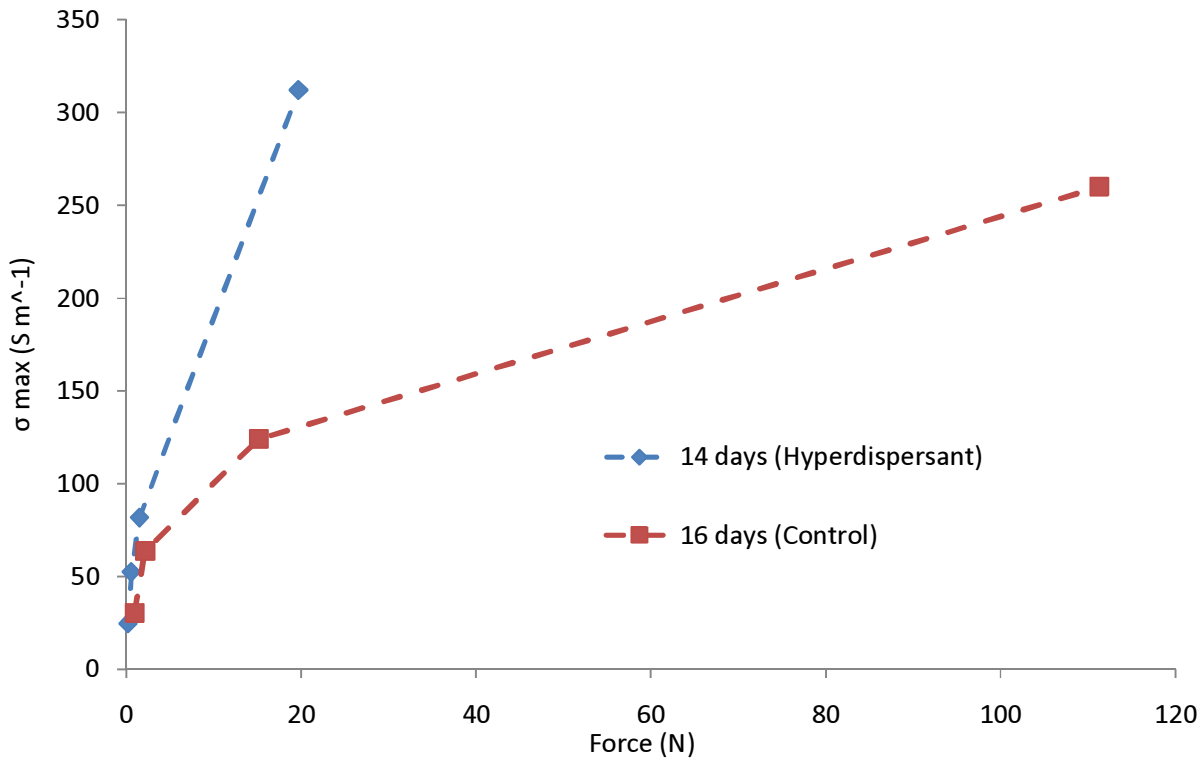

Figure 4. : The response of conductivity to applied force of a low K2 fraction ink (blue) and a low K2 fraction ink with added HD (red). The HD acts to increase touch sensitivity. Dashed lines are added as a guide to the eye.

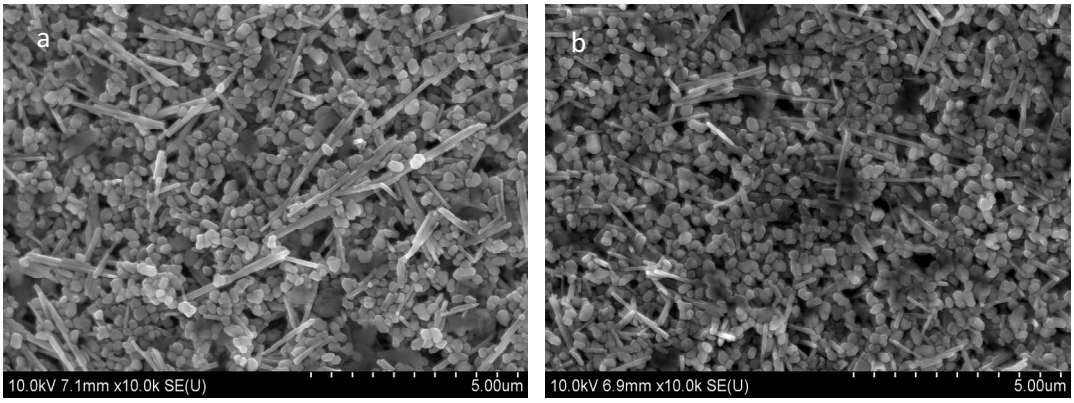

Figure 4. : x10 000 magnification SEM images of (a) low K2 fraction ink with no HD and (b) low K2 fraction ink with added HD.

The apparent affect of HD was then confirmed. HD allows a more even dispersion of K2 particles, breaking up clumps and aggregates. This increases the number of contacts that may form between separate K2 needles when compression of the ink is increased, and counters the effect of lowering the fraction of K2 particles mixed with the base ink.

5. Conclusions

5.1 Summary of Findings

The degradation of pressure sensitivity with ink age, i.e. inks become less conductive with applied pressure when left in storage for a time, may be linked to the growth of small 5 – 10 nm nodules on the surfaces of the K2 needles, likely to affect quantum tunnelling efficiency. The inks have also been found to segregate, either during storage or on printing, possibly into electrically conductive and insulating layers. Voids in the top layer seem to be beneficial to conduction, and these voids slowly disappear with age, reducing ink compressibility and pressure sensitivity. Current-Voltage plots exhibit hysteresis which increases in negativity (ink conductivity is lower during the down ramp of the voltage cycle than it is when the voltage is increased) with greater applied force, before switching to a positive (ink conductivity is higher when the voltage is decreased than when the voltage is increased) value at maximum compression. The negative hysteresis might be a result of charge being trapped and pinching off conduction pathways.

The current-voltage plots can be modelled very well with combined quadratic and linear terms, closely matching behaviour described by NLRRN and DRRN models. The non-linear conductance of the inks initially rises with increasing force, but is reduced at maximum compression. This might be attributed to increasing quantum tunneling from internal field emission as compression increases and brings K2 particles closer together, and a subsequent destruction of quantum tunneling pathways due to the formation of direct contacts between K2 particles. The linear conductance of the inks rises quickly with increasing compression.

The nodules which grow on the K2 needle surfaces appear very swiftly after the K2 is mixed with the base ink, visible after just two days of ink storage time. The development of these nodules, however,

does not seem to depend on the storage temperature, with ink kept at room temperature and refrigerated at 4°C for 58 days both exhibiting the same amount of K2 surface nodules.

Over-blending the inks by injecting the mixture more slowly into a bead mill, which is then operated at a high rpm, has been found to snap and break down K2 needles, lowering the average length of K2 particles by 25% and skewing the distribution of K2 particle dimensions to shorter lengths.

Low K2 fraction inks display lower conductivity in response to applied pressure and are poorer pressure sensors than regular inks. This agrees with Percolation and EM theories; less conductive filler results in fewer possible conduction pathways through the insulating matrix. The addition of hyper-dispersant, an agent which acts to lower viscosity of pressure sensitive ink, was shown to improve the dispersion of K2 particles and lower the tendency of K2 particles to aggregate, reducing the density of clumps of 3 or more K2 particles by 47%

5.2 Suggestions for Future Project Expansion and Continuation

While this research has been largely successful in beginning to understand the nature and operation of pressure sensitive inks, questions remain unanswered. The project could easily be expanded to include more cross sectioning work using FIB milling, first of all, on refrigerated inks to enable more detailed study of the voids present in the layers of ink. Work may also be carried out to ascertain how the distinct layers within the pressure sensitive ink layer form and whether their cause is segregation of particles when the ink is left standing, or if the printing technique controls the ink structure. In addition, ultra-low temperature experiments designed to probe temperature dependent conduction mechanisms and a variety of application tests, such as vapour sensing, could be arranged.

Acknowledgements

The research undertaken as part of this MSc and this subsequent thesis would not have been possible without the greatly appreciated help of my family, namely my parents for their ever present support and guidance, friends and colleagues. I would like to take the opportunity to thank them all for their aid, time and patience.

To begin, I wish to thank OneNorthEast, who kindly provided the financial support for this postgraduate study. Many thanks also go to Dr. Adam Graham, Dr. Paul Laughlin, David Lussey and Professor David Bloor from Peratech Ltd., who all provided invaluable advice, knowledge and all of the pressure sensitive ink samples used in this investigation.

At the Department of Physics at the University of Durham, I would like to thank the members of the Nanoscale Technology and Science and the Photonics, Sensors and Materials research groups, of whom I have been a member of for the course of this MSc. Many thanks go to my academic supervisors, Dr. Graham Cross and Dr. Del Atkinson, who both have provided much guidance and experience in aid of my work. I wish to also extend my gratitude to Mr. Leon Bowen and Dr. Budhika Mendis, who tutored me in the use of the vast electron microscopy facilities available at the University. Furthermore, thanks go to Mr. Duncan McCallum, who has maintained all equipment in the labs to a very high standard.

Finally, I offer my thanks to all my other colleagues at Durham and at Peratech whose support has very much helped the completion of my work.

References

[1] R.H. Norman, “Conductive Rubber” (London: Maclaren), (1957)

[2] M.K Abyaneh and S.K Kulkarni, J. Phys. D: Appl. Phys. 41, p135405, (2008)

[3] M.B. Heaney, Phys. Rev. B. 52, p12477, (1995)

[4] N. Ryvkina et al, Synthetic Metals. 148, p141, (2005)

[5] K. Dai et al, Polymer. 48, p849, (2007)

[6] Q.M Jia et al, Materials Science and Engineering A. 448, p356, (2007)

[7] A. Celzard et al, Phys. Rev. B. 53, p6209, (1996)

[8] Y. Xiong et al, J. Am. Chem. Soc. 127, p7332, (2005)

[9] P.H.C. Camargo et al, J. Am. Chem. Soc. 129, p15452, (2007)

[10] J. Chen et al, Angew. Chem. Int. Ed. 44, p2589, (2005)

[11] X.-S. Yi et al, Polymer International. 44, p117, (1997)

[12] D. Bloor et al, J. Phys: Appl. Phys. 38, p2851, (2005)

[13] D. Bloor et al, Appl. Phys. Lett. 88, 102103, (2006)

[14] www.peratech.com/qtcscience.php viewed on 07/08/2010

[15] S.R. Broadbent, J.M. Hammersley, Proc. Cam. Phil. Soc. 53, p629, (1957)

[16] A. Bunde, W. Dieterich, J. Electroceram. 55, p81, (2000)

[17] I.J. Youngs, J.Phys.D: Appl. Phys. 35, p3127, (2002)

[18] A. Celzard, J.F.Marêché, Physica A. 317, p305, (2003)

[19] A. Graham, Electrical Properties and Vapour Sensing Characteristics of a Novel Metal-Polymer Composite, PhD Thesis, Durham University, (2008)

[20] D.V. Savchenko, S.G. Ionov, J. Phys. Chem. Sol. 71, p548, (2010)

[21] I. Krupa, I. Chodak, Euro. Poly. J. 37, p2159, (2001)

[22] D.S. McLachlan et al, J. Am. Ceram. Soc. 73, p2187, (1990)

[23] http://www.ntmdt.com/spm-basics/view/tunneling-effect (Viewed on 07/08/2010)

[24] R. Eisberg, R. Resnick, "Quantum Physics of Atoms, Molecules, Solids, Nuclei and Particles", Wiley, 2nd Edition, (1985)

[25] R.H. Fowler, L. Nordheim, Proc. R. Soc. Lond. A. 119, p173, (1928)

[26] R.G. Forbes, J.H.B Deane, Proc. R. Soc. A, 463, p2907, (2007)

[27] M.A. Lampert, P. Mark, Elec. Sci. New York and London Academic Press, p351, (1970)

[28] A. Mott, R.W. Gurney, "Electronic Process in Ionic Crystals", Oxford Science Publications, London: Oxford University Press, (1940)

[29] K.W. Böer, "Introduction to Space Charge Effects in Semiconductors", Springer, (2010)

[30] P. Sheng, J. Klafter, Phys. Rev. B. 27, p2583, (1983)

[31] P. Sheng, B. Abeles, Y. Arie, Phys. Rev. Lett. 31, p44, (1973)

[32] A. Celzard et al, J. Phys. : Condens. Matter, 9, p2225, (1997)

[33] A. Celzard et al, J. Mat. Sci. 32, p1849, (1997)

[34] Y. Gefen et al, Phys. Rev. Lett. 57, p3097, (1986)

[35] R.K. Chakrabarty et al, Phys. Rev. B. 44, p6773, (1991)

[36] L. He, S.-C. Tjong, Synthetic Met. (2011), doi:10.1016/j.synthmet.2010.12.007

[37] J. Goldstein et al, "Scanning Electron Microscopy and X-ray Microanalysis", Springer, 3rd Edition, (2003)

[38] http://www4.nau.edu/microanalysis/Microprobe-SEM/Signals.html (Viewed 07/08/2010)

[39] http://cea.com/training/tutorials/aes_instrumention_tutorial/related.php (Viewed 07/08/2010)

[40] C. Vandecasteele, C.B. Block, "Modern Methods for Trace Element Determinations", Wiley, (1997)

[41] http://www.dur.ac.uk/electron.microscopy (Viewed on 07/08/2010)

[42] L.A. Giannuzzi, F.A. Stevie, “Introduction to Focused Ion Beams: Instrumentation, Theory, Techniques and Practice, Springer, 1st Edition, (2005)

[43] http://pprco.tripod.com/SIMS/Theory.htm (Viewed 07/08/2010)

[44] http://www.mauricewilkinscentre.org/bioviz/index.php?page_id=118 (Viewed 07/08/2010)

[45] D.B. Williams, C.B.Carter, “Transmission Electron Microscopy: A textbook for Materials Science”, Springer, 2nd Edition, (2009)

[46] P. Eaton, P. West, “Atomic Force Microscopy”, Oxford University Press, (2010)

[47] I. Horcas et al, Rev. Sci. Instrum. 78, 013705, (2007)